CRREL
REPORT 87-6

US Army Corps of Engineers
Cold Regions Research & Engineering Laboratory

Electromagnetic property trends in sea ice, Part I

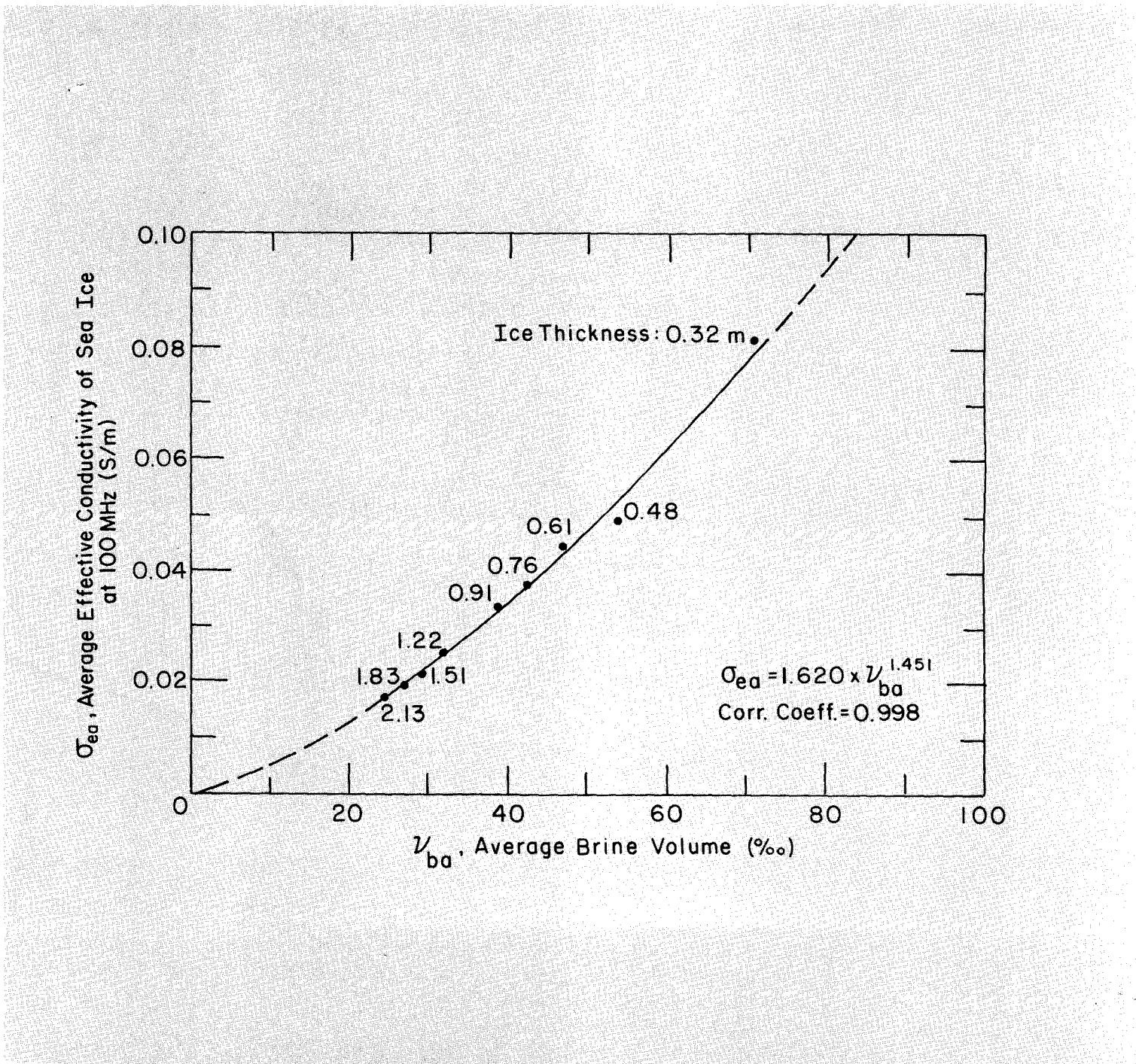

CRREL Report 87-6

April 1987

Electromagnetic property trends in sea ice, Part I

A. Kovacs, R.M. Morey, G.F.N. Cox and N.C. Valleau

Prepared for
U.S. DEPARTMENT OF ENERGY

Unclassified
SECURITY CLASSIFICATION OF THIS PAGE

REPORT DOCUMENTATION PAGE

Form Approved
OMB No. 0704-0188
Exp. Date: Jun 30, 1986

a. REPORT SECURITY CLASSIFICATION Unclassified	1b. RESTRICTIVE MARKINGS
a. SECURITY CLASSIFICATION AUTHORITY	3. DISTRIBUTION/AVAILABILITY OF REPORT Approved for public release; distribution is unlimited.
b. DECLASSIFICATION/DOWNGRADING SCHEDULE	
. PERFORMING ORGANIZATION REPORT NUMBER(S) CRREL Report 87-6	5. MONITORING ORGANIZATION REPORT NUMBER(S)
a. NAME OF PERFORMING ORGANIZATION U.S. Army Cold Regions Research and Engineering Laboratory 6b. OFFICE SYMBOL (If applicable) CRREL	7a. NAME OF MONITORING ORGANIZATION U.S. Department of Energy
c. ADDRESS (City, State, and ZIP Code) Hanover, New Hampshire 03755-1290	7b. ADDRESS (City, State, and ZIP Code) Washington, D.C.
a. NAME OF FUNDING/SPONSORING ORGANIZATION 8b. OFFICE SYMBOL (If applicable)	9. PROCUREMENT INSTRUMENT IDENTIFICATION NUMBER DE-A121-83MC20022
c. ADDRESS (City, State, and ZIP Code)	10. SOURCE OF FUNDING NUMBERS PROGRAM ELEMENT NO. / PROJECT NO. / TASK NO. / WORK UNIT ACCESSION NO.

11. TITLE (Include Security Classification)
Electromagnetic Property Trends in Sea Ice, Part I

12. PERSONAL AUTHOR(S)
Kovacs, A., Morey, R.M., Cox, G.F.N. and Valleau, N.C.

13a. TYPE OF REPORT	13b. TIME COVERED	14. DATE OF REPORT (Year, Month, Day)	15. PAGE COUNT
	FROM _____ TO _____	April 1987	55

16. SUPPLEMENTARY NOTATION
Co-sponsored by the Naval Ocean Research and Development Activity (Contract N6845286MP60003, program element 63704) and the U.S. Coast Guard (MIPR Z51100-5-00004)

17. COSATI CODES			18. SUBJECT TERMS (Continue on reverse if necessary and identify by block number)	
FIELD	GROUP	SUB-GROUP	Electromagnetic properties	Remote sensing
			Polar regions	Sea ice
			Radar	

19. ABSTRACT (Continue on reverse if necessary and identify by block number)
Two-phase dielectric mixing model results are presented showing the electromagnetic (EM) properties of sea ice versus depth. The modeled data are compared with field measurements and show comparable results. It is also shown how the model data can be used in support of impulse radar and airborne electromagnetic (AEM) remote sensing of sea ice. Examples of the remote measurement of sea ice thickness using impulse radar operating in the 80- to 300-MHz frequency band and low-frequency (500 to 30,000 Hz) sounding techniques are presented and discussed.

20. DISTRIBUTION/AVAILABILITY OF ABSTRACT XX UNCLASSIFIED/UNLIMITED ☐ SAME AS RPT. ☐ DTIC USERS	21. ABSTRACT SECURITY CLASSIFICATION Unclassified
22a. NAME OF RESPONSIBLE INDIVIDUAL Austin Kovacs	22b. TELEPHONE (Include Area Code) 603-646-4411 22c. OFFICE SYMBOL CRREL-EA

DD FORM 1473, 84 MAR 83 APR edition may be used until exhausted. All other editions are obsolete.

SECURITY CLASSIFICATION OF THIS PAGE
Unclassified

PREFACE

This report was prepared by Austin Kovacs, Research Civil Engineer, Applied Research Branch, Experimental Engineering Division, and Gordon F.N. Cox, Research Geophysicist, Snow and Ice Branch, Research Division, U.S. Army Cold Regions Research and Engineering Laboratory; Rexford M. Morey, Consultant, Londonderry, New Hampshire; and Nicholas C. Valleau, Geotech Ltd., Markham, Ontario, Canada. Funding for this study was provided by the U.S. Department of Energy under contract no. DE-A121-83MC20022; the U.S. Department of Navy, Naval Ocean Research and Development Activity, under contract no. N6845286MP60003; and in part by the U.S. Coast Guard under MIPR no. Z51100-5-00004.

The authors acknowledge the field assistance provided by Quincy Robe of the U.S. Coast Guard Research and Development Center, Groton, Connecticut; Brian M. Bennett of CRREL; and Chester F. Bassani and Victor R. Cole of Geotech Ltd. They also acknowledge the helpful review of this report by Dr. Gary R. Olhoeft, U.S. Geological Survey, and Dr. Robert G. Onstott, Environmental Research Institute of Michigan; and the advice of Dr. J. Scott Holladay, Geotech Ltd., in relation to the airborne EM survey results.

CONTENTS

ILLUSTRATIONS

TABLES

NOMENCLATURE

A	attenuation (dB/m)
c	free space electromagnetic wave velocity (0.3 m/ns)
D	ice thickness (m)
D_i	ice depth (m)
E_r	relative elastic modulus
F_r	relative flexural strength
f	frequency (Hz)
H_p	primary magnetic field
H_s	secondary magnetic field
I	current
IP	in-phase
j	$\sqrt{-1}$
m	formation factor
N	normality
n	depolarization factor
Rx	receive antenna or coil
Q	quadrature phase
S	conductance (siemens)
S_b	salinity of brine (‰)
S_w	salinity of seawater (‰)
T	temperature (°C)
T_f	freezing temperature of seawater (°C)
T_x	transmit antenna or coil
t	travel time (ns)
V_a	apparent electromagnetic wavelet velocity of propagation (m/ns)
V_m	electromagnetic wave phase velocity of propagation in material (m/ns)
α	real attenuation constant
β	real phase constant
γ	complex propagation constant
ϵ_a	apparent dielectric constant of ice sheet
ϵ_e	real effective dielectric constant
ϵ_o	free space dielectric constant (F/m)
ϵ^*_{rb}	relative complex dielectric constant of brine
$\epsilon'_{rb}, \epsilon''_{rb}$	real and imaginary parts of ϵ^*_{rb}
ϵ^*_{ri}	relative complex dielectric constant of fresh ice
$\epsilon'_{ri}, \epsilon''_{ri}$	real and imaginary parts of ϵ^*_{ri}
ϵ_{rm}	relative dielectric constant of sea ice mixture
ϵ^*_{rm}	relative complex dielectric constant of sea ice mixture
$\epsilon'_{rm}, \epsilon''_{rm}$	real and imaginary parts of ϵ^*_{rm}

$\epsilon_{r\infty}$	relative microwave dielectric constant for seawater
ϵ_{rsb}	relative static dielectric constant of brine
ϵ_{rsi}	relative static dielectric constant of fresh ice
μ_o	free space permeability (H/m)
μ'	real part of magnetic permeability (H/m)
μ_r'	relative real part of magnetic permeability
ν_b	brine volume (‰)
ν_{ba}	average brine volume of ice sheet (‰)
ϱ_w	density of seawater (Mg/m^3)
ϱ_i	density of brine-free ice (Mg/m^3)
σ_e	effective conductivity (S/m)
σ_{ea}	average effective conductivity of ice sheet (S/m)
σ_{DCi}	DC conductivity of sea ice (S/m)
σ_{DCb}	ionic conductivity of brine (S/m)
σ_{NaCl}	conductivity of NaCl solution (S/m)
σ_w	conductivity of sea water
τ	relaxation time (s)
τ_b	relaxation time of brine (s)
τ_i	relaxation time of fresh ice (s)
ω	angular frequency (rad/s)

Electromagnetic Property Trends in Sea Ice, Part I

A. KOVACS, R.M. MOREY, G.F.N. COX AND N.C. VALLEAU

Introduction

The electromagnetic properties of sea ice continue to be a topic of considerable interest to the remote sensing community. Our interests have focused on the remote measurement of sea ice thickness, both from the surface and from low-flying aircraft. We have concentrated on the use of impulse radar operating in the megahertz frequency band.

As a necessity and an outgrowth of this work, the findings of earlier investigators working on sea ice and electromagnetic theory were combined to devise methodology for determining the electromagnetic properties of sea ice in the frequency range of interest. The formulations and models used were assembled to account for the fact that sea ice is a complex, lossy, anisotropic dielectric consisting of pure ice, brine, air and perhaps solid salts. The quantity of these constituent parts is a strong function of seawater salinity and ice growth rate, structure, temperature and age.

Sea ice is classified by age (first-, second- and multi-year) and by morphology. The latter is complicated in that growth (accretion), melt (ablation) and deformation processes can result in ice formations of complex shape, structure, and brine and air content. For example, first-year sea ice may consist of varying amounts of snow ice (snow permeated with refrozen seawater), frazil ice (plate- and needle-shaped ice crystals which become concentrated and freeze together), or congelation ice (normal crystal growth at the ice/water interface as a result of conductive heat loss through the ice to the atmosphere). And multi-year ice may range from layers of congelation ice of varying thicknesses that accreted over a number of growth seasons to a conglomeration of sea ice blocks surrounded by refrozen summer surface melt or solidified seawater. The latter structure occurs when sea ice fails under pressure and forms ridges or rubble. While there are other sea ice morphology variations, those given should serve to indicate that sea ice can take diverse forms.

This paper will concentrate on modeling and illustrating the relative electromagnetic property trends in undeformed first-year sea ice sheets 0.3 to 2.1 m thick. Examples of impulse radar ($\sim$80- to $\sim$300-MHz band) and low-frequency (500- to 30,000-Hz band) airborne electromagnetic sounding techniques and results are presented and discussed.

Sea ice growth and structure

Seawater is a multicomponent electrolyte. It comprises many salts, of which sodium chloride (NaCl) makes up about 78% (Assur 1960) and forms a precipitate beginning at -22.9°C. Another salt precipitate of interest is mirabilite ($Na_2SO_4 \cdot 10H_2O$), which forms when temperatures fall below -8.2°C, a not uncommon sea ice temperature. The salts in seawater depress its freezing point T_f (Kester 1974):

$$T_f = -0.0137 - 0.05199S_w - 0.00007225S_w^2 \quad (1)$$

where T_f is in °C and S_w is the salinity of the seawater in parts per thousand (‰). For most purposes, the simplified expression of Maykut (1985), $T_f = -0.055S_w$, can be used.

The presence of salts also affects seawater density ϱ_w (Defant 1961):

$$\varrho_w = 1 + 0.0008 S_w. \tag{2}$$

In general, when the seawater temperature falls to its freezing point ice begins to form. At first, small needles or disks of ice form. These are called frazil crystals. As these crystals multiply they gradually coalesce and congeal into a slush. In the Arctic Ocean this layer may be very thin (millimeters) or very thick (tens of centimeters), depending upon whether a quiescent (low frazil production) or turbulent (high frazil production) sea state existed at the time of ice formation. For the purposes of this study we assume the frazil ice layer is only a few millimeters thick.

With the formation of the frazil ice layer additional heat loss to the atmosphere from the sea occurs only through the ice. The stage is now set for growth of congelation ice. At first this ice consists of randomly oriented crystals which become more and more ordered and grow wider with depth. This order is brought about by thermodynamic growth processes which favor a preferred geometric orientation. Under this process the ice crystals become vertically elongated as they grow downward. The crystals which predominate are those which have c-axes parallel to the freezing interface. Thus, these axes lie in a horizontal plane.

Each ice crystal consists of a "layered" fresh ice platelet structure, in which the c-axis is perpendicular to the plate or basal plane. The fresh ice platelet may be conceptualized as a glass pane, and the crystal viewed as a stack of glass panes. Between these ice plates is found a series of small, vertical, elongated pockets. These are small inclusions of saline liquid which were trapped as the fresh ice platelets grew into the seawater. As the ice thickens and the trapped saline water cools, fresh water freezes to the ice pocket wall. In this way the remaining liquid becomes enriched with salts and is referred to as brine. The volume of brine in sea ice depends on temperature and is proportional to the liquid salinity at a given temperature.

A plan view depicting the ice crystal structure is shown in Figure 1. It is recognized that the salt in sea ice resides in the brine pockets and that the pockets' liquid volumes and spatial arrangement control to a large degree the electromagnetic and mechanical properties of the ice. The entrapment of brine occurs in the growth or skeletal (SK) layer at the bottom of the ice. A model of this dendritic growth layer and related platelet and brine pocket arrangement is shown in Figure 2. The significance of this layer is that it provides a growth mechanism for trapping saline liquid in the ice. The faster the ice grows the more seawater is trapped. The air shown in the brine pocket in Figure 2 has been found to represent a small void volume, $\leq 5‰$, in first-year ice extending below sea level (Nakawo 1983). For this reason, the air volume is not generally determined. A schematic illustration of the structure of thick sea ice, having a refrozen seawater-infiltrated snow layer on top of which is a layer of snow, is given in Figure 3. This model shows a brine drainage system which aids in the gradual downward migration of liquid from the brine pockets to the seawater. This system has a geometry similar to a tree. The branches of this tree, the brine channels, are inclined between 40° and 54° (Lake and Lewis 1970) but average about 45°. The channels intersect the vertical brine pockets, allowing the pockets to drain down the channels into the larger "trunk" or vertical brine drainage tube which

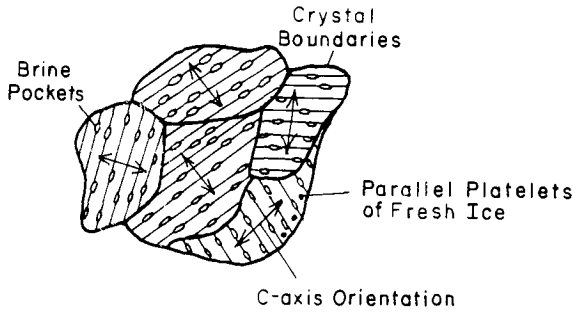

Figure 1. Plan view of sea ice crystal structure.

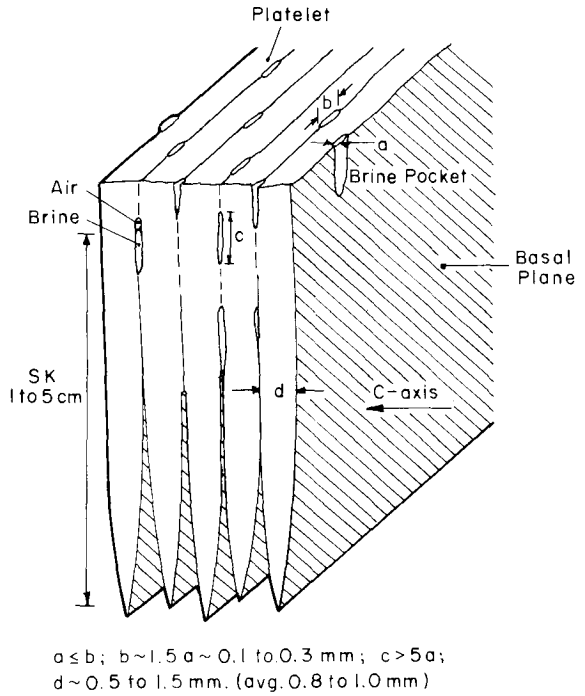

Figure 2. Model of sea ice skeletal (SK) layer structure.

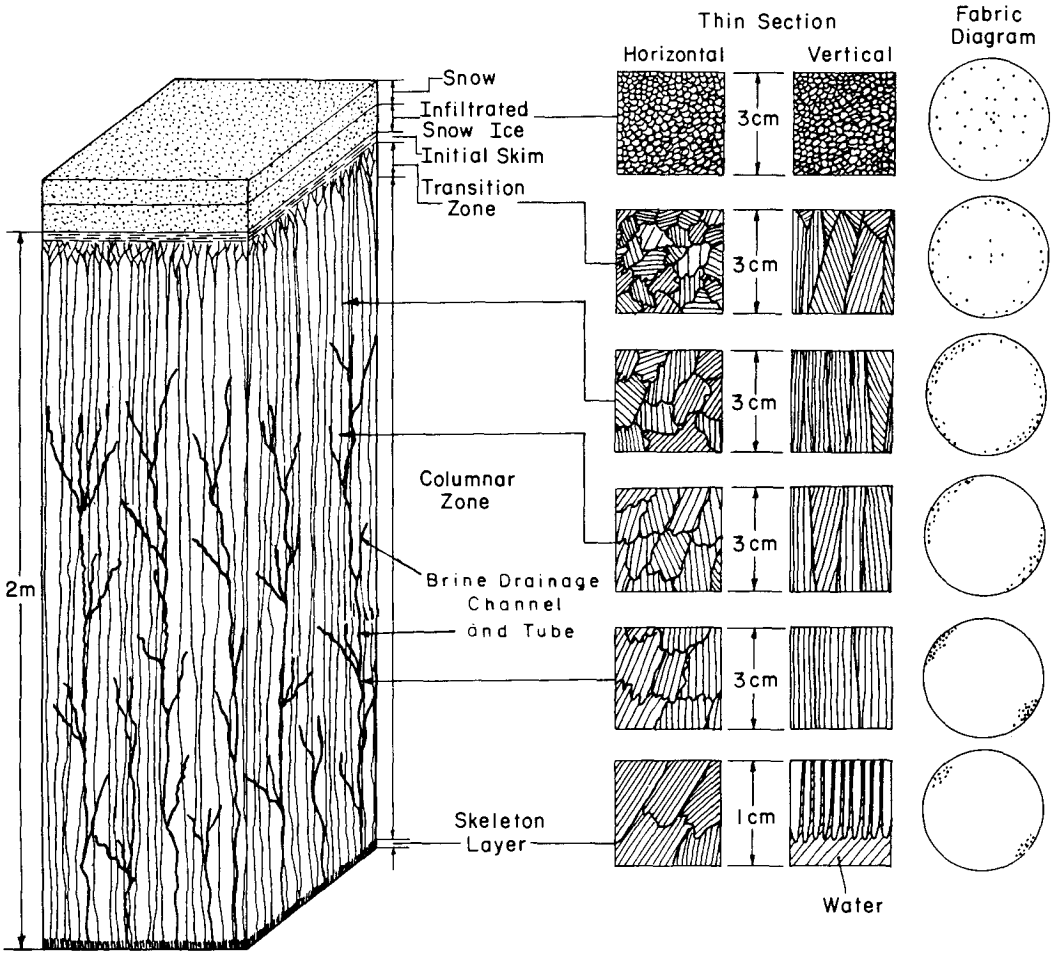

Figure 3. Illustration of first-year sea ice structure with a snow cover (after Schwarz and Weeks 1977). The brine drainage tubes are spaced 5 to 17 cm apart but on average are about 10 cm apart. The brine drainage channels are sloped at 30° to 60° but on average are at about 45°.

leads to the sea. From the observations of Lake and Lewis (1970) and the theoretical modeling of Criminale and Lelong (1984), it appears that brine expulsion from sea ice is optimized when the drainage system is either vertical or tilted at about 45°. We have found the vertical drainage tubes to be spaced 5 to 17 cm apart in sea ice between ½ and 2 m thick, but on the average they are about 10 cm apart.

The growth of sea ice in current-free water results in a structure in which the c-axes of the crystals are randomly oriented, as depicted in Figure 1. However, if a current exists under the ice sheet, selective ice platelet growth occurs in which the c-axis of the crystal becomes aligned with the current (Kovacs and Morey 1978, Weeks and Gow 1979, Langhorne and Robinson 1986). The significance of this alignment is that it renders the ice anisotropic and thus affects the electromagnetic (Kovacs and Morey 1978, 1979; Morey et al. 1984) and mechanical (Payton 1966, Wang 1979, Timco and Frederking 1986) properties of the ice. The modeling presented in this paper assumes that first-year sea ice consists of crystals whose c-axes are randomly oriented in the horizontal plane. The ice is therefore considered isotropic.

Model sea ice

Cox and Weeks (1985) recently modeled the growth versus time and the constituent parts of first-year ice versus depth. In their modeling, they assumed zero air volume in the ice, a linear temperature gradient through the ice, and no snow cover. Their model considered the initial salinity of the ice at formation and its "freshening" due to brine drainage to the sea. The model does not consider the negligible effects of the solid salts which precipitate out at negative temperatures. For example, sodium sulfate decahydrate or mirabilite salt ($Na_2SO_4 \cdot 10H_2O$) begins to precipitate at about -8.2°C, followed by sodium chloride dihydrate or hydrohalite ($NaCl \cdot 2H_2O$) at about -22.9°C. Other salts also precipitate out, but these salts represent only a relatively small percentage, about 20%, of the total quantity found in most seawater, and generally precipitate at lower temperatures, which are seldom of interest.

The model also included the effect of temperature on the bulk density of the ice. Ignored were the constituent properties of the skeletal layer, or about the lower 5 cm of the ice sheet. Cox and Weeks (1985) presented their primary growth model results for ice which began to grow on 1 October. The simulated data are presented in tables and graphs for ice sheet growth in increments of 0.15 m to a total thickness of about 2.1 m. Calculations of ice salinity, temperature and brine volume were made at 1-cm increments. The results of this simulation were found to mimic the constituent property trends found in natural sea ice. Because of this we elected to use this unique data set to model the electromagnetic properties of first-year sea ice of various thicknesses.

We used the sea ice temperature and salinity data of Cox and Weeks (1985), and obtained their unpublished bulk density data versus depth. Then, following the procedures outlined in Cox and Weeks (1983), we calculated the bulk sea ice density in Mg/m^3 at 5-cm depth increments. In these density determinations, the negligible weight and volume effects of the solid salt precipitation were also included. The results are listed in Tables 1–9 and are graphically presented in Figures 4–7. Nine ice sheets were modeled. Figure 4 shows the assumed linear temperature distribution in each ice sheet. Figures 5 and 6 show a decrease in ice salinity and brine volume with increasing ice thickness. Figure 6 shows that beginning with ice sheet 5, about 0.9 m thick, the brine volume curve near the surface has moved left of vertical; it continues to do so with ice sheets of increasing thickness. This response is the result of near-surface ice temperatures dropping below -22.9°C. As previously mentioned, at this temperature the predominant salt in seawater, $NaCl \cdot 2H_2O$, begins to precipitate out. To maintain phase equilibrium a proportionately larger quantity of liquid must freeze to the brine pocket walls. This reduction in brine volume and related increase in ice volume also affects the brine-free ice density as shown in Figure 7. It will be shown that this brine volume and temperature

Table 1. Physical and electromagnetic properties of 0.30-m-thick model ice sheet 1 using NaCl brine conductivities at 100 MHz.

Depth		Ice	Ice	Bulk	Brine	Ice	σ_{DCb}	ε'_{rb}	ε''_{rb}	σ_{DCi}	σ_e	A	ε_{rm}	ε'_{rm}	ε''_{rm}
Depth cm	Incr cm	temp -°C	sal ‰	den_3 Mg/m^3	vol ‰	den_3 Mg/m^3	S/m			S/m	S/m	dB/m			
2.5	0-05	12.6	9.0	.928	42.2	.880	5.70	46.87	1024.31	.038	.038	25.32	6.14	4.20	.038
7.5	5-10	10.6	7.9	.927	42.1	.880	6.09	49.82	1094.56	.041	.041	26.54	6.33	4.20	.036
12.5	10-15	8.6	7.3	.927	45.8	.875	6.37	52.56	1145.86	.048	.049	30.12	7.01	4.27	.036
17.5	15-20	6.6	7.0	.927	54.7	.868	5.98	58.56	1075.13	.060	.061	34.76	8.13	4.48	.046
22.5	20-25	4.6	7.2	.929	77.7	.846	5.10	65.30	917.40	.090	.090	44.52	10.95	4.96	.072
27.5	25-30	2.6	8.6	.937	162.8	.768	3.71	72.87	668.39	.210	.211	72.77	22.52	6.52	.168

Table 2. Physical and electromagnetic properties of 0.46-m-thick model ice sheet 2 using NaCl brine conductivities at 100 MHz.

Depth		Ice	Ice	Bulk	Brine	Ice	σ_{DCb}	ε'_{rb}	ε''_{rb}	σ_{DCi}	σ_e	A	ε_{rm}	ε'_{rm}	ε''_{rm}
Depth cm	Incr cm	temp -°C	sal ‰	den_3 Mg/m^3	vol ‰	den_3 Mg/m^3	S/m			S/m	S/m	dB/m			
2.5	0-05	15.8	8.9	.928	35.5	.887	4.91	41.47	883.03	.025	.025	18.32	5.07	4.05	.038
7.5	5-10	14.1	7.7	.927	33.2	.888	5.35	44.46	961.63	.024	.025	18.10	4.98	3.99	.032
12.5	10-15	12.5	7.1	.926	33.4	.888	5.72	47.02	1028.23	.026	.027	19.25	5.12	4.00	.031
17.5	15-20	10.9	6.7	.926	34.9	.886	6.03	49.39	1085.14	.030	.030	21.19	5.38	4.02	.030
22.5	20-25	9.3	6.5	.926	38.2	.883	6.28	51.62	1130.28	.036	.036	24.32	5.89	4.10	.031
27.5	25-30	7.6	6.4	.926	44.3	.877	6.26	55.33	1124.86	.045	.045	28.67	6.72	4.24	.036
32.5	30-35	6.0	6.3	.927	53.4	.869	5.76	60.53	1036.36	.056	.056	33.04	7.74	4.45	.046
37.5	35-40	4.4	6.6	.928	74.2	.850	4.99	66.02	896.92	.081	.082	41.95	10.21	4.90	.071
42.5	40-45	2.8	7.8	.934	136.6	.792	3.88	72.06	697.99	.166	.167	63.83	18.39	6.08	.144

Table 3. Physical and electromagnetic properties of 0.61-m-thick model ice sheet 3 using NaCl brine conductivities at 100 MHz.

Depth		Ice	Ice	Bulk	Brine	Ice	σ_{DCb}	ε'_{rb}	ε''_{rb}	σ_{DCi}	σ_e	A	ε_{rm}	ε'_{rm}	ε''_{rm}
Depth cm	Incr cm	temp -°C	sal ‰	den_3 Mg/m^3	vol ‰	den_3 Mg/m^3	S/m			S/m	S/m	dB/m			
2.5	0-05	18.5	8.8	.928	31.4	.891	4.17	35.96	750.08	.017	.018	13.62	4.52	3.96	.040
7.5	5-10	17.1	7.6	.927	28.7	.893	4.56	38.95	819.55	.017	.017	13.07	4.41	3.89	.033
12.5	10-15	15.6	7.0	.926	28.1	.893	4.96	41.84	892.59	.017	.018	13.68	4.44	3.87	.030
17.5	15-20	14.2	6.6	.926	28.3	.893	5.32	44.29	957.20	.019	.019	14.67	4.53	3.88	.028
22.5	20-25	12.8	6.4	.925	29.6	.892	5.65	46.56	1016.41	.022	.022	16.36	4.72	3.91	.028
27.5	25-30	11.3	6.2	.925	31.4	.890	5.96	48.81	1071.94	.025	.025	18.44	4.98	3.95	.028
32.5	30-35	9.9	6.1	.925	34.2	.889	6.20	50.80	1114.85	.030	.030	21.14	5.36	4.01	.029
37.5	35-40	8.4	6.0	.925	38.3	.885	6.39	52.83	1149.82	.037	.037	24.66	5.96	4.12	.031
42.5	40-45	7.0	6.0	.926	44.5	.878	6.10	57.27	1097.19	.044	.045	28.26	6.67	4.26	.037
47.5	45-50	5.5	6.0	.926	54.9	.867	5.55	62.20	998.61	.056	.057	33.16	7.80	4.47	.049
52.5	50-55	4.1	6.3	.928	75.6	.848	4.80	67.10	864.45	.081	.081	41.67	10.10	4.92	.074
57.5	55-60	2.7	7.6	.934	138.0	.791	3.80	72.46	683.33	.166	.166	63.62	18.34	6.11	.148

Table 4. Physical and electromagnetic properties of 0.76-m-thick model ice sheet 4 using NaCl brine conductivities.

Depth		Ice	Ice	Bulk	Brine	Ice									
Depth cm	Incr cm	temp -°C	sal ‰	den_3 Mg/m^3	vol ‰	den_3 Mg/m^3	σ_{DCb} S/m	ε'_{rb}	ε''_{rb}	σ_{DCI} S/m	σ_e S/m	A dB/m	ε_{rm}	ε'_{rm}	ε''_{rm}
a. At 100 MHz.															
2.5	0-05	21.1	8.7	.928	28.3	.894	3.48	29.51	625.79	.012	.013	10.00	4.18	3.88	.043
7.5	5-10	19.8	7.5	.927	25.5	.896	3.82	32.90	686.49	.012	.012	9.49	4.08	3.81	.036
12.5	10-15	18.5	6.9	.926	24.6	.897	4.17	35.96	750.08	.012	.012	9.76	4.08	3.79	.032
17.5	15-20	17.2	6.5	.926	24.4	.897	4.53	38.74	814.60	.013	.013	10.41	4.12	3.79	.029
22.5	20-25	15.8	6.3	.925	25.1	.896	4.91	41.47	883.03	.014	.015	11.64	4.21	3.80	.027
27.5	25-30	14.5	6.1	.925	25.8	.895	5.25	43.78	943.74	.016	.016	12.82	4.31	3.82	.026
32.5	30-35	13.2	6.0	.925	27.1	.894	5.56	45.93	1000.14	.018	.019	14.39	4.47	3.85	.026
37.5	35-40	11.9	5.9	.925	28.7	.892	5.84	47.93	1050.83	.021	.021	16.18	4.67	3.88	.026
42.5	40-45	10.5	5.8	.925	31.0	.890	6.10	49.96	1097.60	.025	.025	18.50	4.97	3.94	.027
47.5	45-50	9.2	5.8	.925	34.4	.887	6.30	51.75	1132.66	.030	.031	21.55	5.42	4.02	.028
52.5	50-55	7.9	5.8	.925	38.9	.882	6.32	54.36	1136.37	.037	.037	24.56	6.00	4.12	.032
57.5	55-60	6.6	5.8	.926	45.2	.876	5.98	58.56	1075.13	.045	.045	28.36	6.69	4.26	.038
62.5	60-65	5.2	5.8	.926	55.8	.866	5.41	63.22	973.48	.056	.057	33.14	7.81	4.49	.051
67.5	65-70	3.9	6.2	.928	78.1	.846	4.58	67.83	841.62	.083	.083	42.32	10.39	4.97	.078
72.5	70-75	2.6	7.5	.934	141.6	.787	3.71	72.87	668.39	.168	.169	64.22	18.62	6.16	.153
b. At 80 MHz.															
2.5	0-05	21.1	8.7	.928	28.3	.894	3.48	29.51	782.10	.012	.013	9.84	4.34	3.89	.035
7.5	5-10	19.8	7.5	.927	25.5	.896	3.82	32.90	857.96	.012	.012	9.28	4.22	3.81	.028
12.5	10-15	18.5	6.9	.926	24.6	.897	4.17	35.96	937.42	.012	.012	9.55	4.22	3.79	.025
17.5	15-20	17.2	6.5	.926	24.4	.897	4.53	38.74	1018.08	.013	.013	10.16	4.28	3.79	.023
22.5	20-25	15.8	6.3	.925	25.1	.896	4.91	41.47	1103.59	.014	.014	11.33	4.41	3.80	.022
27.5	25-30	14.5	6.1	.925	25.8	.895	5.25	43.78	1179.48	.016	.016	12.45	4.55	3.82	.021
32.5	30-35	13.2	6.0	.925	27.1	.894	5.56	45.93	1249.97	.018	.018	13.91	4.75	3.85	.021
37.5	35-40	11.9	5.9	.925	28.7	.892	5.84	47.93	1313.31	.021	.021	15.56	5.03	3.88	.021
42.5	40-45	10.5	5.8	.925	31.0	.890	6.10	49.96	1371.78	.025	.025	17.68	5.42	3.94	.021
47.5	45-50	9.2	5.8	.925	34.4	.887	6.30	51.75	1415.59	.031	.031	20.46	6.00	4.02	.023
52.5	50-55	7.9	5.8	.925	38.9	.882	6.32	54.36	1420.21	.037	.037	23.52	6.73	4.12	.025
57.5	55-60	6.6	5.8	.926	45.2	.876	5.98	58.57	1343.64	.045	.045	26.57	7.59	4.26	.031
62.5	60-65	5.2	5.8	.926	55.8	.866	5.41	63.22	1216.55	.056	.056	30.84	8.98	4.49	.041
67.5	65-70	3.9	6.2	.928	78.1	.846	4.58	67.84	1051.71	.081	.081	38.50	11.98	4.98	.063
72.5	70-75	2.6	7.5	.934	141.6	.787	3.71	72.87	835.14	.168	.169	58.52	22.34	6.17	.123

Table 5. Physical and electromagnetic properties of 0.91-m-thick model ice sheet 5 using NaCl brine conductivities at 100 MHz.

Depth		Ice	Ice	Bulk	Brine	Ice									
Depth cm	Incr cm	temp -°C	sal ‰	den_3 Mg/m^3	vol ‰	den_3 Mg/m^3	σ_{DCb} S/m	ε'_{rb}	ε''_{rb}	σ_{DCI} S/m	σ_e S/m	A dB/m	ε_{rm}	ε'_{rm}	ε''_{rm}
2.5	0-05	23.3	8.6	.927	22.9	.899	2.98	22.91	535.42	.008	.008	6.49	3.88	3.76	.041
7.5	5-10	22.1	7.5	.927	23.6	.898	3.24	26.66	582.35	.009	.009	7.31	3.93	3.77	.039
12.5	10-15	20.9	6.8	.926	22.2	.899	3.53	30.06	634.86	.009	.009	7.24	3.89	3.73	.034
17.5	15-20	19.7	6.5	.926	22.2	.899	3.84	33.14	691.30	.009	.009	7.50	3.84	3.65	.030
22.5	20-25	18.4	6.2	.925	22.2	.899	4.20	36.19	755.03	.010	.010	8.50	3.95	3.73	.028
27.5	25-30	17.2	6.0	.925	22.5	.899	4.53	38.74	814.60	.011	.011	9.28	4.00	3.74	.027
32.5	30-35	16.0	5.9	.925	23.3	.898	4.86	41.09	873.40	.013	.013	10.40	4.09	3.76	.026
37.5	35-40	14.8	5.8	.925	24.1	.897	5.17	43.26	930.06	.014	.014	11.52	4.18	3.78	.025
42.5	40-45	13.5	5.7	.925	25.3	.896	5.49	45.44	987.59	.016	.016	12.98	4.32	3.81	.025
47.5	45-50	12.3	5.7	.925	27.1	.894	5.76	47.33	1035.92	.019	.019	14.84	4.51	3.85	.025
52.5	50-55	11.1	5.6	.925	28.7	.892	6.00	49.10	1078.63	.022	.022	16.55	4.71	3.88	.025
57.5	55-60	9.9	5.6	.925	31.3	.890	6.20	50.80	1114.85	.026	.026	18.97	5.03	3.95	.027
62.5	60-65	8.7	5.6	.925	34.7	.886	6.36	52.43	1143.80	.031	.031	21.95	5.48	4.02	.028
67.5	65-70	7.4	5.6	.925	39.6	.882	6.21	55.98	1116.34	.038	.038	25.13	6.04	4.14	.033
72.5	70-75	6.2	5.6	.925	46.1	.876	5.84	59.87	1050.06	.045	.045	28.48	6.74	4.28	.040
77.5	75-80	5.0	5.7	.926	56.9	.866	5.31	63.91	955.66	.057	.057	33.38	7.89	4.53	.053
82.5	80-85	3.8	6.1	.928	78.7	.845	4.61	68.20	829.84	.083	.083	42.24	10.37	4.98	.080
87.5	85-90	2.5	7.4	.935	145.4	.784	3.63	73.28	653.16	.172	.173	64.92	18.97	6.23	.160

Table 6. Physical and electromagnetic properties of 1.22-m-thick model ice sheet 6 using NaCl brine conductivities at 100 MHz.

Depth		Ice	Ice	Bulk	Brine	Ice	σ_{DCb}	ε'_{rb}	ε''_{rb}	σ_{DCl}	σ_e	A	ε_{rm}	ε'_{rm}	ε''_{rm}
Depth cm	Incr cm	temp -°C	sal ‰	den_3 Mg/m^3	vol ‰	den_3 Mg/m^3	S/m			S/m	S/m	dB/m			
2.5	0-05	26.6	8.6	.927	11.2	.910	2.45	22.81	440.61	.002	.002	1.89	3.48	3.47	.025
7.5	5-10	25.6	7.4	.926	11.5	.910	2.61	23.13	469.65	.002	.002	2.08	3.49	3.48	.024
12.5	10-15	24.5	6.8	.926	13.3	.908	2.78	23.45	500.12	.003	.003	2.73	3.54	3.52	.026
17.5	15-20	23.5	6.4	.926	16.1	.905	2.93	23.72	526.72	.004	.004	3.82	3.63	3.59	.030
22.5	20-25	22.4	6.1	.926	19.0	.903	3.17	25.76	570.03	.006	.006	5.23	3.75	3.66	.032
27.5	25-30	21.4	5.9	.925	19.0	.903	3.40	28.69	612.41	.006	.007	5.58	3.76	3.66	.030
32.5	30-35	20.3	5.8	.925	19.4	.902	3.68	31.64	662.69	.007	.007	6.12	3.78	3.67	.028
37.5	35-40	19.3	5.7	.925	19.7	.902	3.95	34.11	710.71	.008	.008	6.76	3.82	3.68	.027
42.5	40-45	18.3	5.6	.925	20.1	.901	4.23	36.41	759.99	.009	.009	7.42	3.85	3.68	.026
47.5	45-50	17.2	5.5	.925	20.6	.900	4.53	38.74	814.60	.010	.010	8.19	3.90	3.69	.024
52.5	50-55	16.2	5.5	.925	21.5	.900	4.80	40.72	863.71	.011	.011	9.18	3.96	3.72	.024
57.5	55-60	15.1	5.4	.924	22.2	.899	5.09	42.74	916.17	.012	.012	10.14	4.04	3.73	.023
62.5	60-65	14.1	5.4	.924	23.2	.898	5.35	44.46	961.63	.014	.014	11.27	4.14	3.76	.023
67.5	65-70	13.1	5.4	.924	24.5	.896	5.58	46.08	1004.26	.016	.016	12.62	4.26	3.78	.023
72.5	70-75	12.0	5.4	.924	26.1	.895	5.82	47.78	1047.16	.018	.018	14.25	4.44	3.82	.024
77.5	75-80	11.0	5.4	.924	27.9	.893	6.02	49.25	1081.91	.021	.021	16.00	4.64	3.86	.025
82.5	80-85	9.9	5.3	.924	29.6	.891	6.20	50.80	1114.85	.024	.024	17.70	4.85	3.90	.025
87.5	85-90	8.9	5.3	.924	32.2	.889	6.34	52.16	1139.51	.028	.028	20.00	5.16	3.97	.027
92.5	90-95	7.8	5.3	.925	35.9	.885	6.30	54.68	1132.70	.033	.033	22.68	5.60	4.05	.030
97.5	95-100	6.8	5.3	.925	40.3	.881	6.04	57.92	1086.53	.038	.038	25.11	6.06	4.15	.034
102.5	100-105	5.8	5.4	.925	47.1	.875	5.68	61.20	1021.87	.045	.045	28.58	6.77	4.31	.042
107.5	105-110	4.7	5.4	.926	57.0	.865	5.16	64.95	927.30	.056	.056	32.79	7.77	4.52	.054
112.5	110-115	3.7	5.8	.928	76.8	.847	4.55	68.58	817.82	.078	.079	40.87	9.99	4.94	.079
117.5	115-120	2.6	6.8	.933	128.1	.800	3.71	72.87	668.39	.144	.145	58.59	16.31	5.93	.144

Table 7. Physical and electromagnetic properties of 1.51-m-thick model ice sheet 7 using NaCl brine conductivities at 100 MHz.

Depth		Ice	Ice	Bulk	Brine	Ice	σ_{DCb}	ε'_{rb}	ε''_{rb}	σ_{DCl}	σ_e	A	ε_{rm}	ε'_{rm}	ε''_{rm}
Depth cm	Incr cm	temp -°C	sal ‰	den_3 Mg/m^3	vol ‰	den_3 Mg/m^3	S/m			S/m	S/m	dB/m			
2.5	0-05	28.1	8.6	.927	9.1	.913	2.19	22.28	394.17	.001	.001	1.26	3.43	3.43	.023
7.5	5-10	27.2	7.4	.926	8.8	.913	2.35	22.61	422.48	.001	.001	1.27	3.42	3.42	.021
12.5	10-15	26.4	6.8	.926	9.1	.912	2.48	22.88	446.53	.001	.002	1.40	3.42	3.42	.020
17.5	15-20	25.5	6.4	.925	10.1	.911	2.63	23.16	472.48	.002	.002	1.72	3.45	3.44	.021
22.5	20-25	24.6	6.1	.925	11.6	.910	2.77	23.42	494.41	.002	.003	2.21	3.50	3.48	.023
27.5	25-30	23.7	5.9	.925	14.0	.907	2.90	23.66	521.48	.003	.004	3.06	3.57	3.54	.026
32.5	30-35	22.8	5.7	.925	17.5	.904	3.08	24.52	554.19	.005	.005	4.51	3.69	3.62	.031
37.5	35-40	21.9	5.6	.925	17.7	.904	3.28	27.24	590.76	.006	.006	4.86	3.70	3.63	.029
42.5	40-45	21.1	5.5	.925	17.8	.904	3.48	29.51	625.79	.006	.006	5.18	3.72	3.64	.028
47.5	45-50	20.2	5.5	.925	18.4	.903	3.71	31.89	667.41	.007	.007	5.77	3.75	3.65	.027
52.5	50-55	19.3	5.4	.925	18.7	.903	3.95	34.11	710.71	.007	.007	6.26	3.77	3.66	.026
57.5	55-60	18.4	5.4	.925	19.3	.902	4.20	36.19	755.03	.008	.008	6.95	3.81	3.67	.025
62.5	60-65	17.5	5.3	.925	19.6	.901	4.45	38.12	799.73	.009	.009	7.50	3.84	3.67	.024
67.5	65-70	16.6	5.3	.924	20.3	.901	4.69	39.94	844.19	.010	.010	8.28	3.90	3.69	.023
72.5	70-75	15.8	5.3	.924	21.1	.900	4.91	41.47	883.03	.011	.011	9.13	3.96	3.71	.023
77.5	75-80	14.9	5.3	.924	21.9	.899	5.15	43.09	925.45	.012	.012	10.05	4.03	3.72	.023
82.5	80-85	14.0	5.2	.924	22.5	.898	5.37	44.63	966.03	.013	.013	10.85	4.09	3.74	.022
87.5	85-90	13.1	5.2	.924	23.6	.897	5.58	46.08	1004.26	.015	.015	11.99	4.20	3.76	.023
92.5	90-95	12.2	5.2	.924	24.8	.896	5.78	47.48	1039.70	.017	.017	13.23	4.32	3.79	.023
97.5	95-100	11.3	5.2	.924	26.3	.894	5.96	48.81	1071.94	.019	.019	14.70	4.48	3.82	.023
102.5	100-105	10.5	5.1	.924	27.3	.893	6.10	49.96	1097.60	.021	.021	15.74	4.60	3.85	.024
107.5	105-110	9.6	5.1	.924	29.2	.892	6.24	51.21	1122.80	.023	.023	17.48	4.82	3.90	.025
112.5	110-115	8.7	5.1	.924	31.6	.889	6.36	52.43	1143.80	.027	.027	19.60	5.11	3.95	.026
117.5	115-120	7.8	5.1	.924	34.5	.886	6.30	54.68	1132.70	.031	.031	21.64	5.43	4.01	.028
122.5	120-125	6.9	5.1	.925	38.3	.883	6.07	57.59	1091.95	.035	.035	23.77	5.81	4.10	.033
127.5	125-130	6.0	5.1	.925	43.2	.878	5.76	60.53	1036.36	.040	.040	26.23	6.29	4.21	.038
132.5	130-135	5.2	5.1	.925	49.0	.873	5.41	63.22	973.48	.046	.046	28.81	6.86	4.35	.046
137.5	135-140	4.3	5.2	.926	59.6	.863	4.93	66.37	886.33	.057	.057	33.29	7.53	4.58	.059
142.5	140-145	3.4	5.6	.928	80.4	.844	4.34	69.71	780.23	.080	.081	41.46	10.22	5.02	.086
147.5	145-150	2.5	6.6	.933	129.4	.799	3.63	73.28	653.16	.143	.144	58.36	16.25	5.96	.148

Table 8. Physical and electromagnetic properties of 1.83-m-thick model ice sheet 8 using NaCl brine conductivities at 100 MHz.

Depth		Ice	Ice	Bulk	Brine	Ice	σ_{DCb}	ε'_{rb}	ε''_{rb}	σ_{DCI}	σ_e	A	ε_{rm}	ε'_{rm}	ε''_{rm}
Depth cm	Incr cm	temp -°C	sal o/oo	den$_3$ Mg/m^3	vol o/oo	den$_3$ Mg/m^3	S/m			S/m	S/m	dB/m			
2.5	0-05	28.7	8.6	.927	8.6	.913	2.08	22.04	374.47	.001	.001	1.11	3.41	3.41	.023
7.5	5-10	28.0	7.4	.926	8.0	.914	2.21	22.32	397.38	.001	.001	1.04	3.40	3.40	.020
12.5	10-15	27.2	6.8	.926	8.1	.913	2.35	22.61	422.48	.001	.001	1.12	3.40	3.40	.019
17.5	15-20	26.5	6.4	.925	8.5	.913	2.47	22.84	443.58	.001	.001	1.25	3.41	3.41	.019
22.5	20-25	25.7	6.1	.925	9.3	.912	2.60	23.10	466.81	.002	.002	1.50	3.43	3.43	.020
27.5	25-30	25.0	5.9	.925	10.3	.911	2.70	23.30	486.45	.002	.002	1.81	3.46	3.45	.021
32.5	30-35	24.2	5.7	.925	11.9	.909	2.83	23.53	508.20	.003	.003	2.35	3.50	3.49	.023
37.5	35-40	23.5	5.6	.925	14.1	.907	2.93	23.71	526.72	.003	.004	3.12	3.57	3.54	.026
42.5	40-45	22.7	5.5	.925	16.9	.905	3.10	24.83	558.09	.005	.005	4.31	3.67	3.61	.030
47.5	45-50	22.0	5.4	.925	17.0	.904	3.26	26.95	586.54	.005	.005	4.55	3.67	3.61	.028
52.5	50-55	21.2	5.4	.925	17.5	.904	3.45	29.24	621.30	.006	.006	5.01	3.70	3.62	.027
57.5	55-60	20.5	5.3	.925	17.6	.904	3.63	31.12	653.32	.006	.006	5.30	3.71	3.63	.026
62.5	60-65	19.7	5.3	.925	18.1	.903	3.84	33.14	691.30	.007	.007	5.82	3.74	3.64	.025
67.5	65-70	19.0	5.3	.925	18.5	.903	4.03	34.92	725.40	.007	.007	6.28	3.77	3.65	.025
72.5	70-75	18.2	5.2	.924	18.7	.902	4.25	36.63	764.96	.008	.008	6.71	3.78	3.65	.024
77.5	75-80	17.5	5.2	.924	19.2	.902	4.45	38.12	799.73	.009	.009	7.28	3.82	3.66	.023
82.5	80-85	16.7	5.2	.924	19.9	.901	4.67	39.75	839.28	.010	.010	8.02	3.87	3.68	.023
87.5	85-90	16.0	5.1	.924	20.1	.901	4.86	41.09	873.40	.010	.010	8.44	3.90	3.68	.022
92.5	90-95	15.3	5.1	.924	20.7	.900	5.04	42.38	906.80	.011	.011	9.10	3.95	3.70	.022
97.5	95-100	14.5	5.1	.924	21.5	.899	5.25	43.78	943.74	.012	.012	9.97	4.01	3.71	.022
102.5	100-105	13.8	5.0	.924	21.8	.899	5.42	44.96	974.74	.013	.013	10.46	4.05	3.72	.022
107.5	105-110	13.0	5.0	.924	22.8	.898	5.61	46.24	1008.35	.014	.014	11.49	4.14	3.75	.022
112.5	110-115	12.3	5.0	.924	23.7	.897	5.76	47.33	1035.92	.016	.016	12.40	4.23	3.77	.022
117.5	115-120	11.5	5.0	.924	24.9	.896	5.92	48.52	1065.08	.017	.017	13.58	4.35	3.80	.022
122.5	120-125	10.8	4.9	.924	25.6	.895	6.05	49.53	1088.34	.018	.018	14.36	4.43	3.81	.022
127.5	125-130	10.0	4.9	.924	27.2	.893	6.18	50.66	1112.10	.021	.021	15.84	4.60	3.84	.023
132.5	130-135	9.3	4.9	.924	28.8	.892	6.28	51.62	1130.28	.023	.023	17.27	4.79	3.88	.024
137.5	135-140	8.5	4.8	.924	30.3	.890	6.38	52.69	1147.87	.025	.025	18.66	4.97	3.92	.025
142.5	140-145	7.8	4.8	.924	32.5	.888	6.30	54.68	1113.70	.028	.028	20.13	5.19	3.97	.027
147.5	145-150	7.0	4.8	.924	35.6	.885	6.10	57.27	1097.19	.031	.031	21.90	5.49	4.04	.030
152.5	150-155	6.3	4.8	.924	38.9	.882	5.88	59.54	1056.62	.035	.035	23.63	5.80	4.12	.034
157.5	155-160	5.5	4.8	.925	43.9	.878	5.55	62.20	998.61	.040	.040	25.97	6.27	4.23	.040
162.5	160-165	4.8	4.8	.925	49.6	.872	5.21	64.60	936.97	.045	.045	28.42	6.80	4.36	.048
167.5	165-170	4.0	4.8	.926	58.8	.864	4.74	67.46	853.16	.054	.054	31.93	7.64	4.56	.061
172.5	170-175	3.3	5.2	.927	76.8	.847	4.26	70.10	767.19	.073	.074	39.13	9.57	4.94	.084
177.5	175-180	2.5	6.1	.932	119.5	.808	3.63	73.28	653.16	.126	.127	54.21	14.66	5.78	.140

Table 9. Physical and electromagnetic properties of 2.13-m-thick model ice sheet 9 using NaCl brine conductivities at 100 MHz.

Depth		Ice	Ice	Bulk	Brine	Ice	σ_{DCb}	ε'_{rb}	ε''_{rb}	σ_{DCI}	σ_e	A	ε_{rm}	ε'_{rm}	ε''_{rm}
Depth cm	Incr cm	temp -°C	sal ‰	den_3 Mg/m^3	vol ‰	den_3 Mg/m^3	S/m			S/m	S/m	dB/m			
2.5	0-05	30.4	8.6	.927	7.5	.914	1.75	21.30	314.67	.001	.001	.79	3.38	3.38	.023
7.5	5-10	29.7	7.4	.926	6.7	.915	1.89	21.62	340.05	.001	.001	.71	3.37	3.36	.019
12.5	10-15	29.0	6.8	.926	6.6	.915	2.03	21.92	364.36	.001	.001	.73	3.36	3.36	.018
17.5	15-20	28.3	6.4	.925	6.6	.915	2.16	22.20	387.68	.001	.001	.77	3.36	3.36	.017
22.5	20-25	27.6	6.1	.925	6.9	.915	2.28	22.46	410.07	.001	.001	.86	3.37	3.37	.017
27.5	25-30	27.0	5.9	.925	7.2	.914	2.38	22.68	428.59	.001	.001	.95	3.38	3.37	.017
32.5	30-35	26.3	5.7	.925	7.8	.914	2.50	22.91	449.47	.001	.001	1.11	3.40	3.40	.017
37.5	35-40	25.6	5.6	.925	8.7	.913	2.61	23.13	469.65	.001	.002	1.36	3.42	3.41	.018
42.5	40-45	24.9	5.5	.925	9.8	.911	2.72	23.33	489.20	.002	.002	1.69	3.44	3.43	.020
47.5	45-50	24.2	5.4	.925	11.3	.910	2.83	23.53	508.20	.002	.002	2.17	3.49	3.48	.022
52.5	50-55	23.6	5.3	.925	12.9	.908	2.91	23.69	524.10	.003	.003	2.72	3.53	3.51	.024
57.5	55-60	22.9	5.3	.925	15.9	.906	3.06	24.20	550.34	.004	.005	3.89	3.64	3.59	.028
62.5	60-65	22.2	5.2	.925	16.3	.905	3.22	26.36	578.21	.005	.005	4.23	3.65	3.60	.027
67.5	65-70	21.5	5.2	.925	16.6	.905	3.38	28.40	608.01	.005	.005	4.54	3.67	3.60	.027
72.5	70-75	20.8	5.2	.925	17.0	.904	3.56	30.32	639.44	.006	.006	4.94	3.68	3.61	.026
77.5	75-80	20.2	5.1	.925	17.1	.904	3.71	31.89	667.41	.006	.006	5.18	3.69	3.61	.025
82.5	80-85	19.5	5.1	.924	17.5	.904	3.90	33.63	700.98	.006	.007	5.62	3.72	3.63	.024
87.5	85-90	18.8	5.1	.924	18.0	.903	4.09	35.28	735.25	.007	.007	6.12	3.75	3.63	.024
92.5	90-95	18.1	5.1	.924	18.4	.903	4.28	36.85	769.92	.008	.008	6.59	3.78	3.64	.023
97.5	95-100	17.4	5.0	.924	18.6	.902	4.47	38.33	804.69	.008	.008	6.98	3.79	3.64	.022
102.5	100-105	16.8	5.0	.924	19.0	.902	4.64	39.55	834.36	.009	.009	7.45	3.82	3.66	.022
107.5	105-110	16.1	5.0	.924	19.6	.901	4.83	40.90	868.56	.010	.010	8.10	3.87	3.67	.022
112.5	110-115	15.4	4.9	.924	19.8	.901	5.02	42.20	902.08	.010	.010	8.51	3.89	3.68	.021
117.5	115-120	14.7	4.9	.924	20.5	.900	5.20	43.44	934.65	.011	.011	9.24	3.95	3.69	.021
122.5	120-125	14.0	4.8	.924	20.8	.900	5.37	44.63	966.03	.012	.012	9.71	3.98	3.70	.021
127.5	125-130	13.4	4.8	.924	21.4	.899	5.52	45.61	991.81	.013	.013	10.37	4.04	3.71	.021
132.5	130-135	12.7	4.8	.924	22.3	.898	5.67	46.71	1020.38	.014	.014	11.25	4.11	3.73	.021
137.5	135-140	12.0	4.7	.924	22.7	.898	5.82	47.78	1047.16	.015	.015	11.80	4.16	3.74	.021
142.5	140-145	11.3	4.7	.924	23.8	.897	5.96	48.81	1071.94	.016	.016	12.86	4.27	3.77	.021
147.5	145-150	10.6	4.7	.924	24.9	.896	6.09	49.82	1094.56	.018	.018	13.92	4.38	3.80	.022
152.5	150-155	10.0	4.6	.924	25.5	.895	6.18	50.66	1112.10	.019	.019	14.56	4.45	3.81	.022
157.5	155-160	9.3	4.6	.924	27.0	.894	6.28	51.62	1130.28	.021	.021	15.90	4.61	3.85	.023
162.5	160-165	8.6	4.6	.924	28.7	.892	6.37	52.56	1145.86	.023	.023	17.40	4.80	3.88	.024
167.5	165-170	7.9	4.5	.924	30.1	.890	6.32	54.36	1136.37	.025	.025	18.37	4.93	3.91	.025
172.5	170-175	7.2	4.5	.924	32.5	.888	6.16	56.62	1107.12	.027	.027	19.77	5.15	3.97	.028
177.5	175-180	6.6	4.5	.924	35.0	.886	5.98	58.56	1075.13	.030	.030	21.12	5.38	4.03	.030
182.5	180-185	5.9	4.5	.924	38.6	.882	5.72	60.86	1029.22	.033	.033	22.93	5.69	4.10	.033
187.5	185-190	5.2	4.5	.924	43.2	.878	5.41	63.22	973.48	.038	.038	25.03	6.10	4.21	.041
192.5	190-195	4.6	4.5	.925	48.4	.873	5.10	65.30	917.40	.042	.043	27.23	6.57	4.33	.048
197.5	195-200	3.8	4.7	.926	60.5	.862	4.61	68.20	829.84	.055	.055	32.28	7.74	4.60	.064
202.5	200-205	3.2	5.0	.927	76.1	.848	4.19	70.48	753.88	.071	.072	38.34	9.37	4.93	.085
207.5	205-210	2.5	6.0	.931	117.5	.810	3.63	73.28	653.16	.123	.123	53.36	14.34	5.74	.138

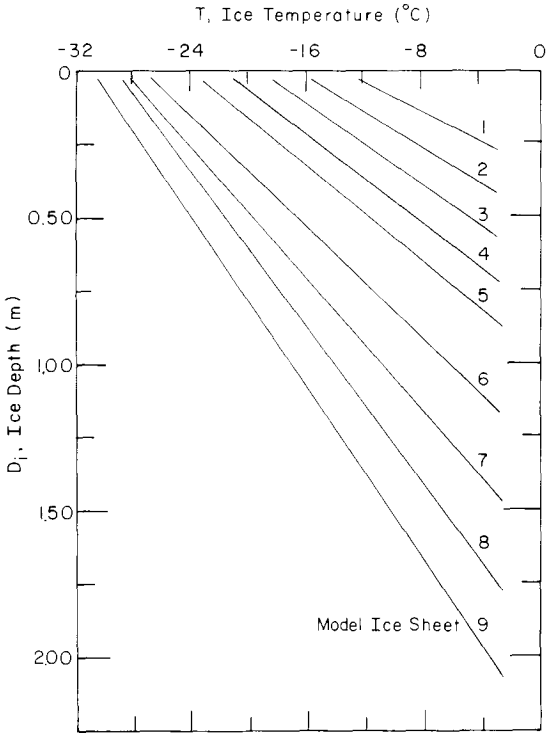

Figure 4. Temperature versus depth in nine model ice sheets.

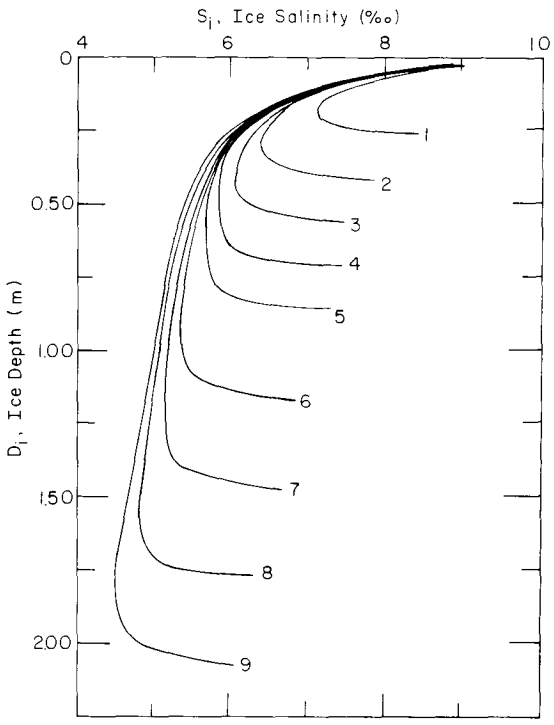

Figure 5. Salinity versus depth in nine model ice sheets.

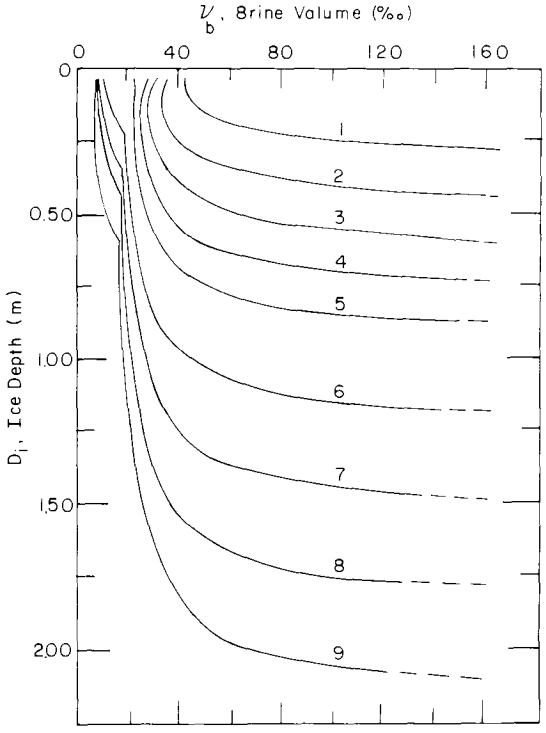

Figure 6. Brine volume versus depth in nine model ice sheets.

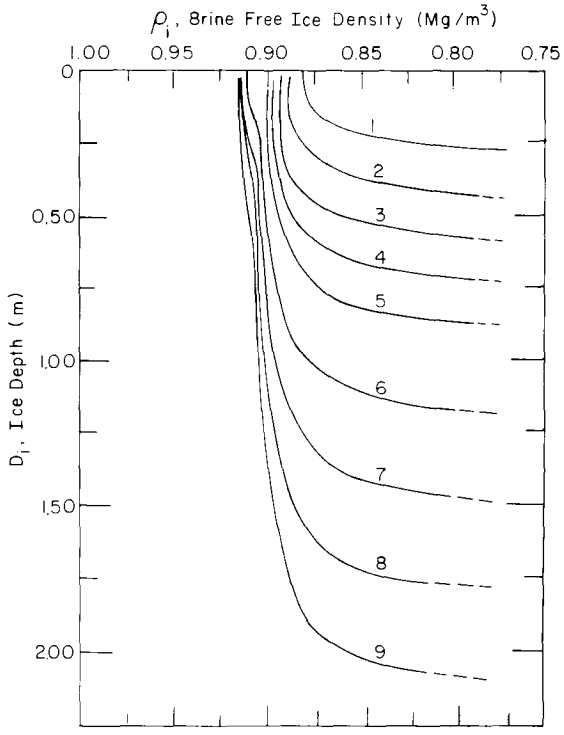

Figure 7. Brine-free ice density versus depth in nine model ice sheets.

decrease also affect the electromagnetic properties of the ice, since it is the brine volume and the mobility of the ions in the brine which affect the conductivity of the ice.

Brine salinity

There is a unique relationship between the salinity of the brine trapped in sea ice and its temperature. The salinity of the brine is always in phase equilibrium with its ice environment, in that the solution is always at the freezing point of the liquid. For example, if the temperature of the ice, and therefore brine, decreases, freezing of a portion of the brine liquid will occur to bring the brine salinity into phase equilibrium with the surrounding ice. Conversely, should the temperature increase, the excessive brine salinity will cause melting of the surrounding ice until once again the brine and ice are in thermal and phase equilibrium. Because of this chemical, thermal and ice phase equilibrium relationship, the salinity of the brine in sea ice can be related to its in situ temperature as shown in Figure 8. Curves A-D represent brine salinity versus temperature based upon the work of Assur (1960). The curves fit his data with a correlation coefficient of about 0.99. In this report we used equations A, B and D because there is a break in the related curve at about -8.2°C, the temperature at which $Na_2SO_4 \cdot 10H_2O$ salt precipitates out of the solution.

Curve E represents NaCl brine salinity versus temperature. This curve shows that below about -14°C, NaCl brine has an appreciably higher salinity than seawater brine. The curve is also seen to terminate at -22.9°C where it is assumed the liquid freezes due to the NaCl salt having precipitated out at this temperature.

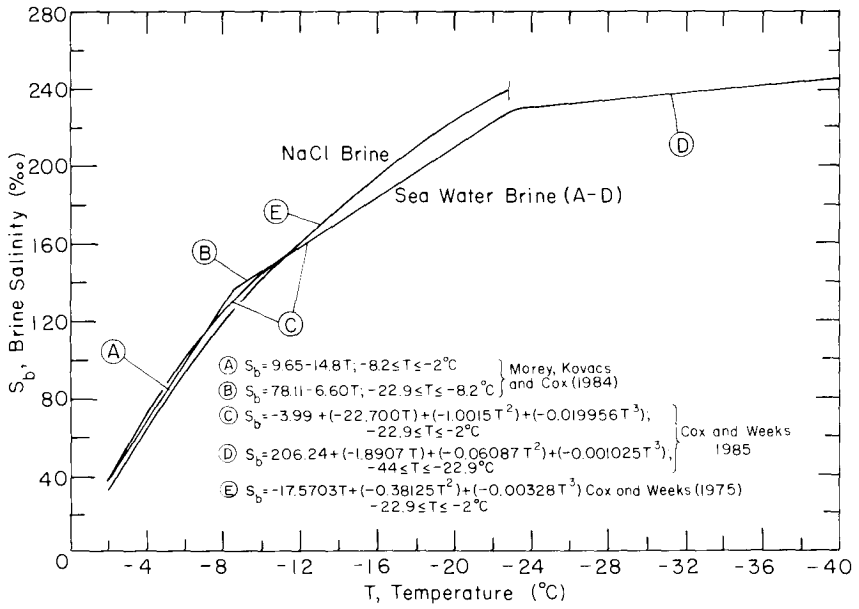

Figure 8. Brine salinity versus temperature.

Seawater and model brine conductivity

The ionic conductivity of seawater is a function of its salt content and temperature. This is graphically shown in Figure 9, which is based upon the tabulated data of Tiphane and St.-Pierre (1962). Since the temperature and salinity of winter Beaufort Sea surface water are about -1.8°C and 32‰, it can be determined from the equation for σ_{DC} (32‰) given in Figure 9 that the conductivity of this seawater is ≈ 2.5 S/m. It was previously shown that when seawater is trapped in sea ice and cooled, it begins to freeze, forming a brine which must be at the freezing point of the liquid and thus in thermal equilibrium with the surrounding ice.

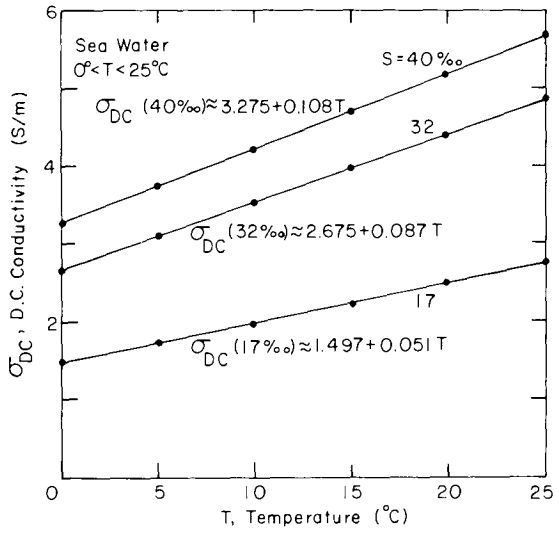

Figure 9. DC conductivity of seawater versus temperature with salinity as parameter.

The result is that as the salinity of the brine increases with decreasing temperature (Fig. 8) the ionic conductivity of the brine increases. This increase can be expected due to an increase in ion concentration in the higher salinity brine. However, Morey et al. (1984) showed that below about -8.2°C the conductivity of the brine decreased with decreasing temperature, even as the brine salinity increased (Fig. 8). They suggested that this effect was "due to a reduction in ionic mobility in the brine caused by the lower temperature and high ion concentration" and that "there are fewer ions available to conduct current because they have recombined to form solid salt crystals."

The above brine conductivity trend as a function of negative temperature was discovered through the use of expressions for the conductivity of concentrated NaCl solutions, σ_{NaCl}. Their use of these expressions was necessitated because at that time there was little information available on the conductivity of brine at low temperatures. The equations used were from Stogryn (1971):

$$\sigma_{NaCl}(T,N) = \sigma_{NaCl}(25,N)[1.000 - 1.962\times10^{-2}\Delta + 8.08\times10^{-5}\Delta^2 - \Delta N\{3.02\times10^{-5} + 3.922\times10^{-5}\Delta + N(1.721\times10^{-5} - 6.584\times10^{-6}\Delta)\}] \quad (3)$$

where $\Delta = 25 - T$ (T = temperature, °C) and

$$\sigma_{NaCl}(25,N) = N[10.394 - 2.3776N + 0.68258N^2 - 0.13538N^3 + 1.0086\times10^{-2}N^4] \quad (4)$$

and normality N is

$$N = S_b[1.707\times10^{-2} + 1.205\times10^{-5}S_b + 4.058\times10^{-9}S_b^2] \quad (5)$$

where S_b = brine salinity (‰).

In their analyses, Morey et al. (1984) used sea ice brine salinity, determined for the sea ice they studied, for the NaCl brine salinity in eq 5. The effect of this is a slight reduction in the conductivity calculated from eq 3 for brine salinities above about 160‰. Following this same procedure we calculated the relative brine conductivity in sea ice versus temperature as graphically shown in Figure 10. The curve shows that 32‰ salinity seawater freezes at about -1.8°C and that 40‰ salinity seawater freezes at about -2.2°C. As fresh ice forms, the remaining liquid becomes salinity-enriched, causing its conductivity to increase. Below a temperature of about -8°C, the brine conductivity is seen to decrease with decreasing temperature, apparently due to a decrease in ionic mobility. At -22.9°C the solid curve is terminated since eq 3 is for an NaCl solution which can be expected to freeze at about this temperature. However, since seawater brine contains a small quantity of other salts which will remain in a saline solution below -22.9°C, it is reasonable to assume that the remaining brine conductiv-

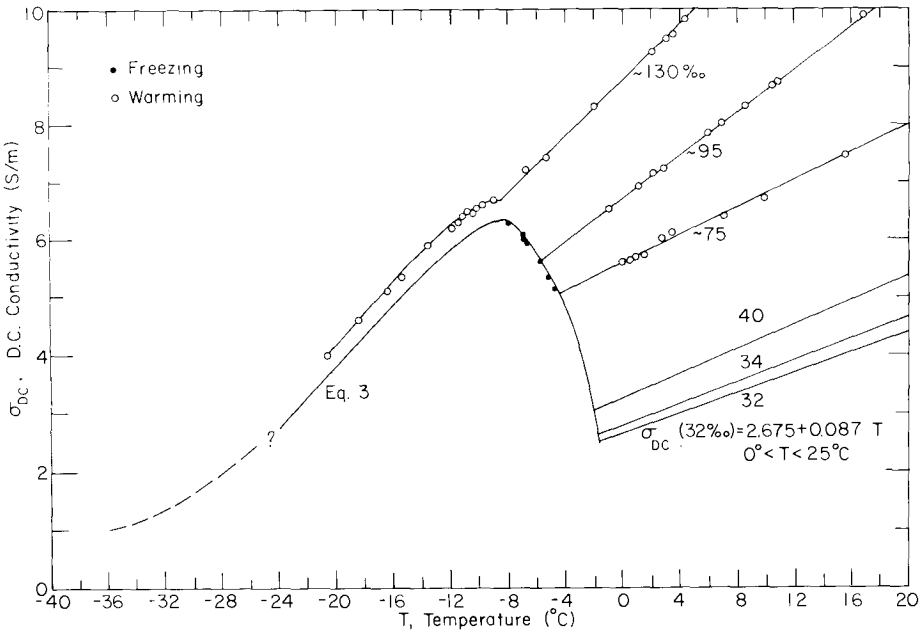

Figure 10. DC conductivity of brine (≥40‰ salinity) and seawater versus temperature.

ity will continue to decrease with temperature and approach zero at about -54°C when virtually all seawater salts have precipitated out. This expected brine conductivity trend is depicted by the dashed curve in Figure 10.

Morey et al. (1984) recognized that eq 3-5 were being used beyond the temperature range for which they were derived, and that sea ice brine contained a variety of salts with different ions than in an NaCl solution, ions that may influence the conductivity versus temperature values calculated from eq 3. A laboratory test was therefore made in 1983 (unpublished) to verify the relative shape of the curve and the conductivity versus temperature values given in Figure 10. Beaufort Sea water was obtained and slowly cooled down to -12°C. During this cooling, the conductivity of the unfrozen liquid, under the growing ice sheet, was measured versus temperature. The results confirmed that the shape of the conductivity versus temperature curve in Figure 10 was quite correct. However, the measured condutivity values for the seawater brine were found to be slightly higher than those represented by the curve in Figure 10 at temperatures below about -8°C. This result was not unexpected since seawater has a variety of salts with ionic mobility at negative temperatures differing from that of an NaCl solution. It was also found that since the quantity of brine in sea ice below -8°C was very small, the net effect of the increased brine conductivity, as determined from the laboratory study, on the effective conductivity and complex dielectric constant of the sea ice was also very small, less than 5%.

The above laboratory study was repeated for this study, wherein Atlantic Ocean water was cooled down to -20.6°C. This was undertaken to better verify the trend depicted in Figure 10. The results are plotted as solid and open circles in Figure 10. The solid circles represent brine conductivity values determined during freezing of the seawater, whereas the open circles represent values determined for the brine forming during warming of the sea ice. Once again, the laboratory results gave higher brine conductivities below about -8°C. This increase in brine conductivity was again found to have little effect on the electromagnetic properties of the model sea ice.

The three rectilinear curves, without data points, at the bottom right in Figure 10 were constructed from the data of Tiphane and St.-Pierre (1962), whereas the three upper curves represent the conductivity of brine, extracted during warming of the sea ice, as it warmed to

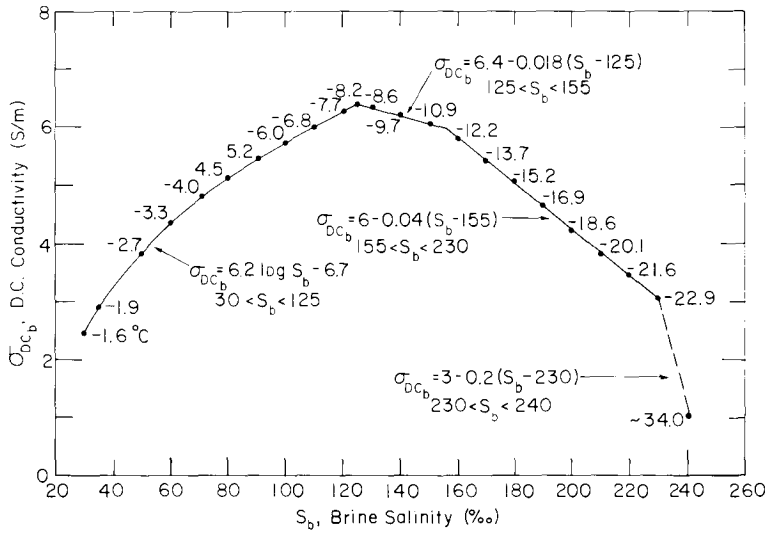

Figure 11. DC conductivity of model brine versus seawater brine salinity with temperature as a parameter.

room temperature. The relative brine salinities represented by these curves may be estimated from Figure 8 to be about 75, 95 and 130‰ respectively in ascending order.

Equations A, B and D in Figure 8 can be combined with eq 3 to express brine conductivity versus brine salinity with temperature as a parameter, as shown in Figure 11. The dashed line is an assumed approximation of the brine conductivity between -22.9° and -34°C following the reasoning previously expressed. The knee in the curve between the temperatures of -10.9° and -12.2°C is an artifact of curve fitting. A smooth transition should exist. In our brine conductivity determinations, the equations given in Figure 11 were used. The relative brine conductivity versus depth in the nine model sea ice sheets is shown in Figure 12. The

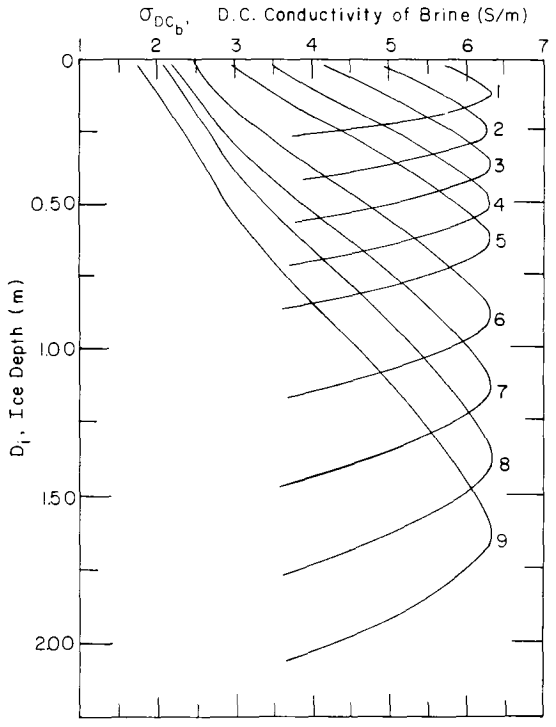

Figure 12. DC conductivity of model brine versus depth in nine model ice sheets.

brine conductivity increases with depth due to increasing ice temperature until about 6.4 S/m where the temperature in the ice is about -8 °C. At this depth, the brine conductivity decreases due to increasing temperature following the trend depicted in Figure 10.

Complex dielectric constant of brine

With reservations previously expressed, equations given by Stogryn (1971) for NaCl solutions were used to approximate the relative static dielectric constant ϵ_{rsb} and the relaxation time τ_b of the sea ice brine at negative temperatures. As given in Morey et al. (1984), the above parameters were calculated as follows:

$$\epsilon_{rsb}(T,N) = \epsilon_{rsb}(T,0)[1.000 - 0.2551N + 5.151 \times 10^{-2}N^2 - 6.889 \times 10^{-3}N^3] \quad (6)$$

and

$$\tau_b(T,N) = \tau_b(T,0)[0.1463 \times 10^{-2}\, NT + 1.000 - 0.04896N - 0.02967N^2 + 5.644 \times 10^{-3}N^3] \quad (7)$$

where

$$\tau_b(T,0) = 17.80 \times 10^{-12} - 0.6032 \times 10^{-12}T + 0.0109 \times 10^{-12}T^2 - 0.0001 \times 10^{-12}T^3 \quad (8)$$

and

$$\epsilon_{rsb}(T,0) = 88.22 - 0.4105T + 0.0008T^2 + 1.0879 \times 10^{-6}T^3. \quad (9)$$

The relative complex dielectric constant of the model sea ice brine ϵ^*_{rb} was then determined using values of ϵ_{rsb} calculated from eq 6 and equations in Figure 11 for σ_{DCb} in the following Debye formula:

$$\epsilon^*_{rb} = \epsilon'_{rb} - j\epsilon''_{rb} = \epsilon_{r\infty} + \frac{\epsilon_{rsb} - \epsilon_{r\infty}}{1 + j\omega\tau_b} - j\,\frac{\sigma_{DCb}}{\omega\epsilon_o} \quad (10)$$

which for our calculations is

$$\epsilon'_{rb} = \frac{\epsilon_{rsb} + \epsilon_{r\infty}\omega^2\tau_b^2}{1 + \omega^2\tau_b^2}$$

and

$$\epsilon''_{rb} = \frac{\omega\tau_b(\epsilon_{rsb} - \epsilon_{r\infty})}{1 + \omega^2\tau_b^2} + \frac{\sigma_{DCb}}{\omega\epsilon_o}$$

where ϵ'_{rb} = relative real dielectric constant of brine
ϵ''_{rb} = relative imaginary dielectric constant of brine
ϵ_{rsb} = relative static dielectric constant of brine (temperature- and salinity-dependent)
$\epsilon_{r\infty}$ = relative microwave dielectric constant for seawater ($\epsilon_{r\infty}$ = 5.5; King and Smith 1981)
ϵ_o = free-space dielectric constant = 8.854×10^{-12} (F/m)
τ_b = relaxation time of brine (temperature- and salinity-dependent)
σ_{DCb} = ionic conductivity of brine (S/m).

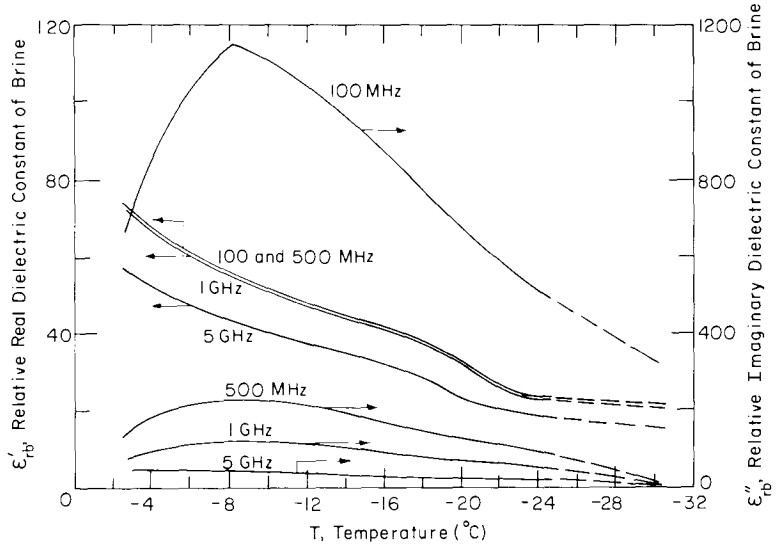

Figure 13. Complex dielectric constant of model brine versus temperature with frequency as a parameter.

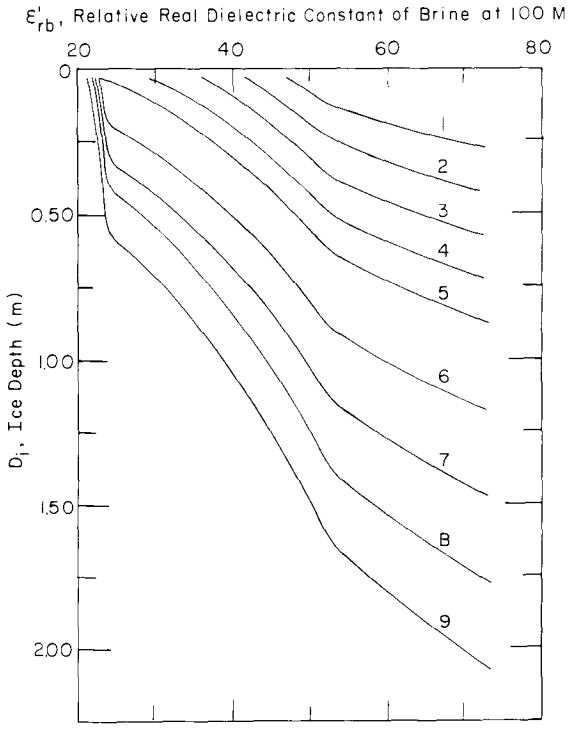

Figure 14. Relative real dielectric constant of model brine at 100 MHz versus depth in nine model ice sheets.

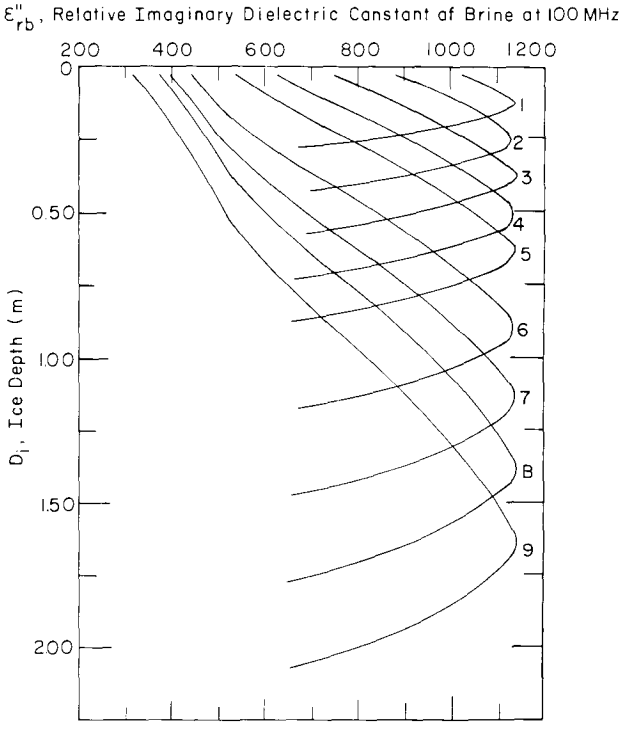

Figure 15. Relative imaginary dielectric constant of model brine at 100 MHz versus depth in nine model ice sheets.

The real and imaginary parts of the relative complex dielectric constant of the model sea ice brine at frequencies of 100 and 500 MHz and at 1 and 5 GHz versus temperature are graphically presented in Figure 13. The dashed lines in this figure represent calculations based upon the extrapolation of the conductivity versus brine salinity curve as shown in Figure 11 between the temperatures of -22.9° and -34°C. Depicted in Figures 14 and 15 are respectively the trends of ϵ'_{rb} and ϵ''_{rb} at 100 MHz versus depth in the model sea ice sheets. ϵ''_{rb} is shown

to vary with ice depth and therefore temperature in the same fashion as did σ_{DCb} (Fig. 12), while ϵ'_{rb} is seen to increase with depth in part under the influence of increasing brine volume (Fig. 6).

Electromagnetic properties of model sea ice at 100 MHz

As used by Kovacs and Morey (1986), the propagation of electromagnetic energy in sea ice can be described by the complex propagation constant γ as

$$\gamma = \alpha + j\beta \tag{11}$$

where the real attenuation constant α is defined as

$$\alpha = \omega\left(\frac{\mu'\epsilon_e}{2}\right)^{1/2}\left[\left(1+\frac{\sigma_e^2}{\omega^2\epsilon_e^2}\right)^{1/2}-1\right]^{1/2} \tag{12}$$

and the real phase constant β is

$$\beta = \omega\left(\frac{\mu'\epsilon_e}{2}\right)^{1/2}\left[\left(1+\frac{\sigma_e^2}{\omega^2\epsilon_e^2}\right)^{1/2}+1\right]^{1/2} \tag{13}$$

where $\omega = 2\pi f$ = angular frequency (rad/s)
f = frequency (Hz)
μ' = real part of magnetic permeability = $\mu_o(= 4\pi\times10^{-7}$ H/m$)\times\mu'_r$
μ'_r = relative real part of the magnetic permeability = 1 for sea ice
ϵ_e = real effective dielectric constant $\approx \epsilon_o\times\epsilon'_{rm}$
ϵ'_{rm} = relative real dielectric constant of sea ice mixture
σ_e = effective conductivity (S/m)
$j = \sqrt{-1}$.

As the electromagnetic wave propagates through the ice with a phase velocity

$$V_m = \omega/\beta \quad \text{(m/ns)} \tag{14}$$

it suffers an exponential attenuation A of

$$A = 20\alpha \log e \quad \text{(dB/m)}$$

$$= 8.686\alpha. \tag{15}$$

The dielectric constant and attenuation of electromagnetic energy in sea ice can be estimated from the temperature, salinity and brine-free density of the ice, and some knowledge of the ice structure. As previously stated, sea ice is a multi-component medium. Its constituent parts are fresh ice, liquid brine, air and, depending upon eutectic factors, solid salt crystals. The volume of fresh ice is by far the larger fraction, typically in excess of 95%. Since the solid salt precipitate, when present, is of such a small volume and influence, it can be ignored. This is generally true for the air volume in first-year sea ice for the frequencies discussed in this report. This volume was not estimated by Cox and Weeks (1985), and is therefore not considered in this modeling presentation.

The Debye equation for determining the relative complex dielectric constant ϵ_{ri}^{*} of the fresh ice platelets is

$$\epsilon_{ri}^{*} = \epsilon_{ri}' - j\epsilon_{ri}'' = 3.14 + \frac{\epsilon_{rsi} - 3.14}{1 + j\omega\tau_i} \tag{16}$$

where ϵ_{rsi} is the relative static dielectric constant, and τ_i is the relaxation time of the ice. Graphics provided by Morey et al. (1984) show these well-established values versus temperature.

The relative real (ϵ_{rm}') and imaginary (ϵ_{rm}'') parts of the relative complex dielectric constant of the sea ice mixture ϵ_{rm}^{*} (ice and brine) can be estimated from the dielectric mixing formula of Tinga et al. (1973):

$$\epsilon_{rm}^{*} = \epsilon_{rm}' - j\epsilon_{rm}'' = \epsilon_{ri}^{*} + \left[\frac{\nu\epsilon_{ri}^{*}(\epsilon_{rb}^{*} - \epsilon_{ri}^{*})}{n(1-\nu)(\epsilon_{rb}^{*} - \epsilon_{ri}^{*}) + \epsilon_{ri}^{*}}\right] \tag{17}$$

where ϵ_{rm}^{*} = relative complex dielectric constant of the mixture (sea ice)
ϵ_{ri}^{*} = relative complex dielectric constant of pure ice (≈ 3.14 for $f > 10^5$ Hz)
ϵ_{rb}^{*} = relative complex dielectric constant of brine
ν_b = brine volume
n = depolarization factor.

The depolarization factor n is a function of the sea ice structure and the orientation of an external electric field relative to the structure. In particular, it is considered a measure of both the shape and the orientation of the brine inclusions with respect to the electric field.

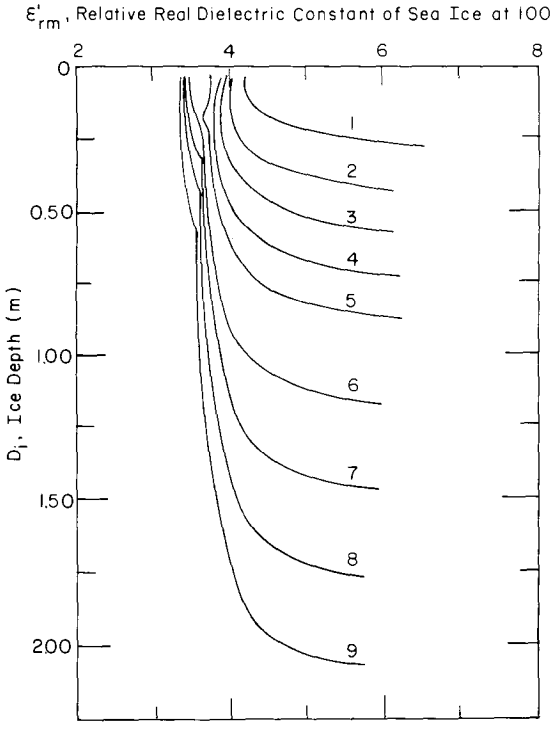

Figure 16. Relative real dielectric constant of model sea ice at 100 MHz versus depth.

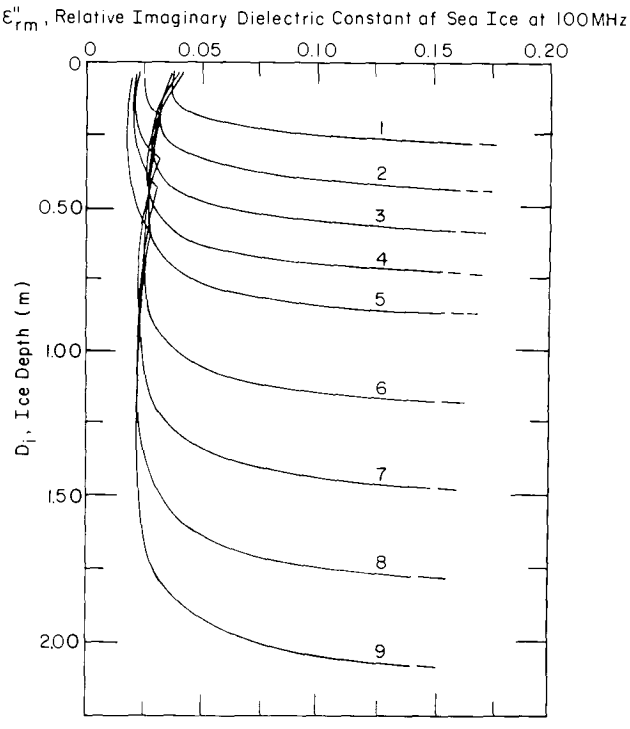

Figure 17. Relative imaginary dielectric constant of model sea ice at 100 MHz versus depth.

From field studies on first-year sea ice, Morey et al. (1984) found n versus depth to cluster around 0.1. This value was therefore used in the above equation. ϵ'_{rm} and ϵ''_{rm} versus depth, for the model ice sheets, are shown in Figures 16 and 17. Both figures show similar trends. ϵ'_{rm} and ϵ''_{rm} increase gradually with depth to where the temperature increases above -8°C (Fig. 4) and more importantly where the brine volume undergoes a rapid increase (Fig. 6). Indeed the ϵ'_{rm} and ϵ''_{rm} curves follow quite well the trend of ν_b and ϱ_i versus depth as shown in Figures 6 and 7. As can be inferred from Figure 17, the sea ice becomes increasingly lossy as the ice temperature and brine volume increase.

The relative real dielectric constant of the sea ice, ϵ'_{rm}, as determined from eq 17, was used to determine ϵ_e in eq 12 and 13. Also, the effective conductivity σ_e of the ice was determined from

$$\sigma_e = \sigma_{DCi} + \omega\epsilon''_{rm}\epsilon_o \tag{18}$$

where σ_{DCi} is the DC conductivity of the ice as determined by Morey et al. (1984):

$$\sigma_{DCi} = \sigma_{DCb}(\nu_b)^m \quad (S/m). \tag{19}$$

Here σ_{DCb} was determined from Figure 11, ν_b is the brine volume of the ice, and m is a formation variable which has to do with porosity and pore water conductivity. Morey et al. (1984) found m to vary between about 1.5 and 1.8. In a recent note, Sen (1984) indicated that m and n are interrelated as follows:

$$m = \frac{5-3n}{3(1-n^2)} \quad . \tag{20}$$

Therefore, since a value of 0.1 was used for n in eq 17, an m value of 1.582, as calculated from eq 20, was used in eq 19.

It was found that the σ_{DCi} and σ_e values were virtually the same. This is in agreement with Addison (1969), who measured the apparent resistivity of saline ice between 20 Hz and 1 MHz and found the resistivity to be relatively independent of frequency. Therefore, the conductivity versus depth in the model ice sheets as shown in Figure 18 is representative of the 0 to 100 MHz frequency band. Here, too, the conductivity is seen to increase with depth, following again the trend of the brine volume curves in Figure 6. This is to be expected since the conductivity of the ice is related to the volume and the temperature of the brine in the ice.

The attenuation of the electromagnetic wave in the model sea ice (Fig. 19) was determined by using σ_e and ϵ_e in eq 12 and the resulting α value in eq 15. As would be expected, the attenuation versus depth for the model ice sheets shows an exponential

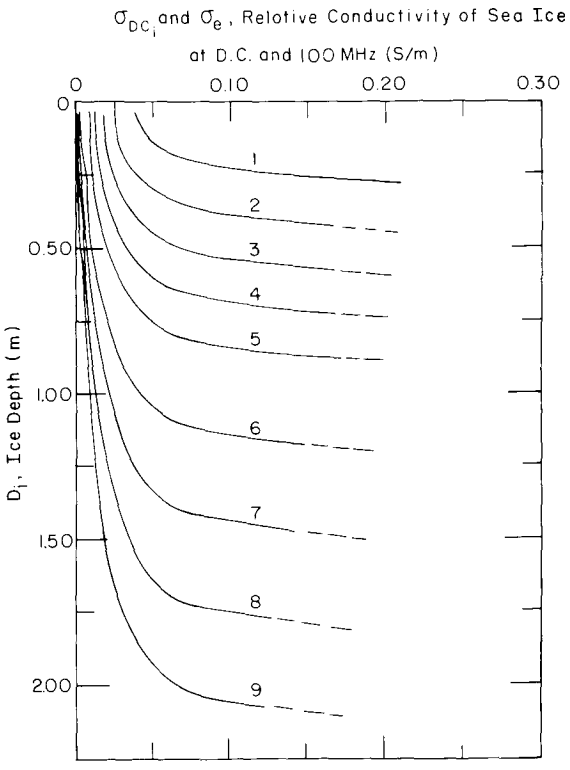

Figure 18. Relative conductivity of model sea ice at 100 MHz versus depth.

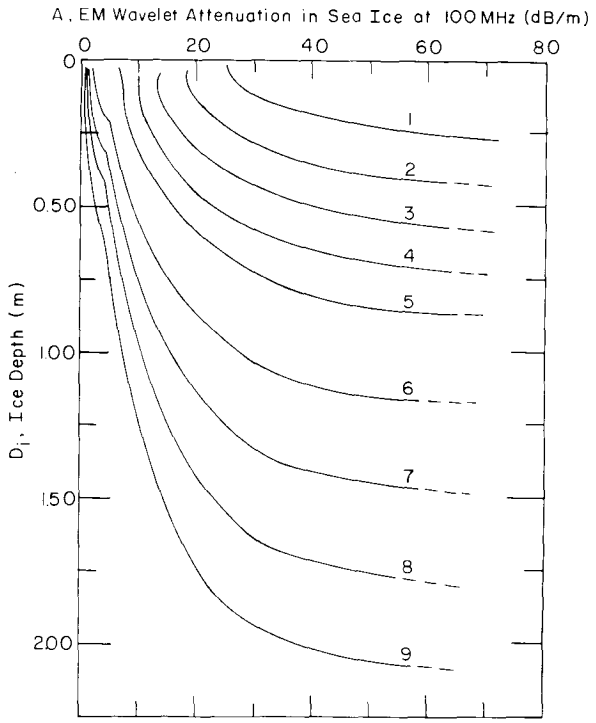

Figure 19. Attenuation in model sea ice at 100 MHz versus depth.

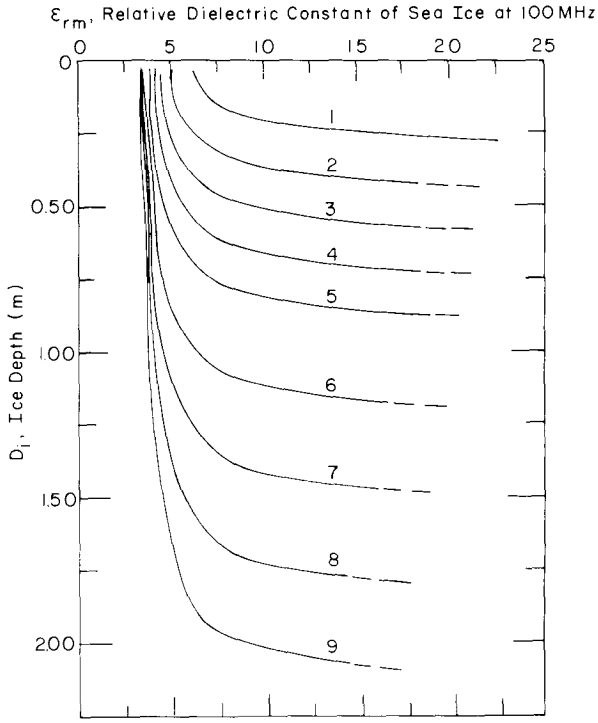

Figure 20. Relative dielectric constant of model sea ice at 100 MHz versus depth.

increase with depth as the temperature and brine volume of the ice increased. It is also apparent that the thinner ice is more lossy, due to its higher temperature and higher brine volume (Fig. 4 and 6).

When an "impulse" radar system is used to sound the thickness of sea ice, it is desirable to know the apparent velocity V_a of the electromagnetic wavelet in the ice, since only the two-way time of flight t is measured. This time is that taken by the wavelet to travel from the ice surface to the "bottom" reflector and back to the surface. Thus if V_a is known, the depth D to the reflecting horizon can be estimated from

$$D = (V_a t/2). \tag{21}$$

The relative incremental depth velocity in the model sea ice mixture, V_m, was first determined by using σ_e and ϵ_e in eq 13 to find the real phase constant β. This value was then used in eq 14 to calculate V_m, the relative phase velocity of an electromagnetic wave of a given frequency propagating under the effect of the ice conductivity. The incremental V_m values were then averaged to obtain V_a, and from eq 21 the relative two-way EM wave travel time within each model ice sheet was calculated. These results will be discussed later.

To determine a relative incremental dielectric constant of the sea ice mixture ϵ_{rm}, V_m was used in the expression

$$\epsilon_{rm} = (c/V_m)^2 \tag{22}$$

where c = free space electromagnetic velocity, 0.3 m/ns. An apparent dielectric constant ϵ_a for each ice sheet was then determined by averaging the incremental ϵ_{rm} values.

A plot of ϵ_{rm} versus ice depth for each ice sheet is given in Figure 20. ϵ_{rm} and ϵ'_{rm} are similar for sea ice having a "low" effective conductivity. For σ_e higher than about 0.003 S/m and

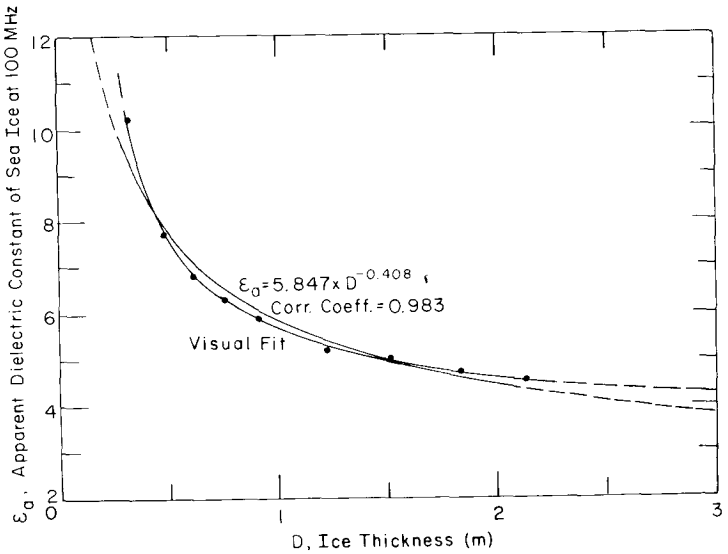

Figure 21. Apparent dielectric constant of model sea ice at 100 MHz versus ice sheet thickness.

a frequency of 100 MHz, ϵ_{rm} increases with respect to ϵ'_{rm}, substantially so near the bottom of the ice sheet, as may be seen by comparing Figures 16 and 20. The curves show ϵ_{rm} to increase exponentially near the bottom of the ice sheet following the increase in brine volume shown in Figure 6. The curves also indicate that for the thicker ice ϵ_{rm} remains relatively constant for about 75% of the ice thickness before rapidly increasing. The implication is that ϵ_a may reach a relatively constant value for thick winter sea ice.

This is further suggested in the plot of ϵ_a versus ice thickness in Figure 21. The power equation given was found to statistically fit the data better than a polynomial, exponential, logarithmic or square root curve. Nonetheless, the visual curve fit through the data track the data best and, when extended as shown, provides more acceptable ϵ_a values. It would appear from this figure that ϵ_a will reach a relatively constant value at some ice thickness in excess of 3 m. This may be assessed by comparing the model ice ϵ_a values with those determined for first- and multi-year ice studied by the authors in 1985. In this study the two-way flight time was measured in ice from 1½ to 7½ m thick. An impulse radar system was used with a wavelet spectrum center frequency of about 80 MHz. Using the two-way travel times and related measured ice thickness in eq 21, the apparent velocity of the electromagnetic wavelet in the ice was calculated. Then using these V_a values in eq 22 an apparent dielectric constant ϵ_a of the ice was determined. One hundred drill hole measurements of ice thickness versus two-way travel time were analyzed and a least-squares curve with a correlation coefficient of 0.92 fitted to the ϵ_a versus ice thickness data (report in preparation). This curve is presented in Figure 22. Also shown are the model ice ϵ_a data and the curve passing through them. The trends of the two curves are in remarkably good agreement, implying that the model results do mimic the electromagnetic properties of sea ice. As for ϵ_a approaching a constant value for thick winter ice, the curve passing through the field data indicated that this occurs when the ice thickness is about 6 m. At this thickness $\epsilon_a \cong 3.47$. For impulse radar sounding of cold winter sea ice at frequencies of about 80 MHz it appears that one can assume $\epsilon_a \cong 3.5$ for ice over 4 m thick. This trend is in agreement with data provided by Bogorodsky (1980) which indicate that, for sea ice thicker than 4 m, ϵ_a reaches a constant value of about 3.9. However, the frequency at which his data were obtained was not given.

Although the forms of the two curves in Figure 22 are similar, there is some difference in the ϵ_a values for the thinner model ice. The lower ϵ_a values for the model ice may be due to

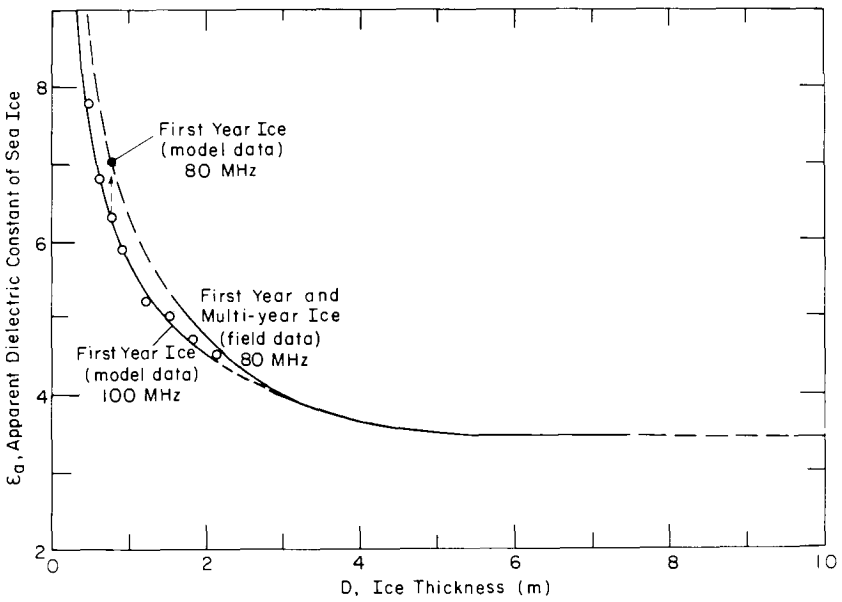

Figure 22. Apparent dielectric constant of model and natural sea ice versus ice sheet thickness with frequency as a parameter.

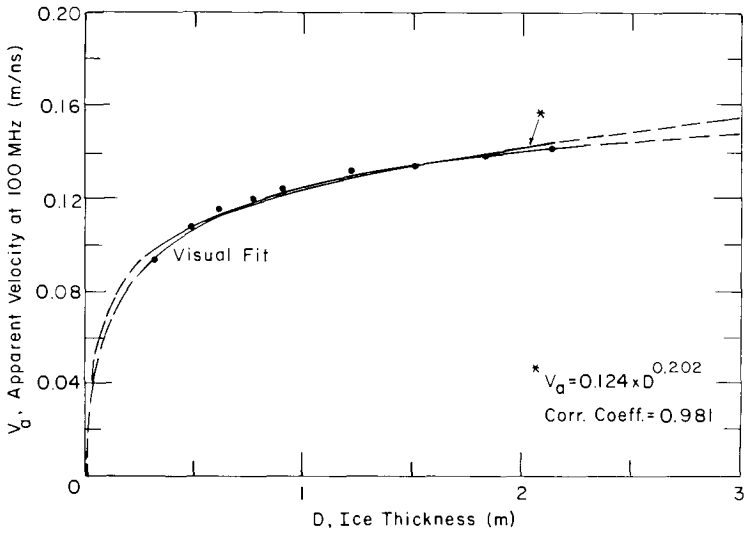

Figure 23. Effective velocity of 100-MHz wave in model sea ice versus ice sheet thickness.

the physical properties used for the model ice sheets, or may be the result of using equations developed for NaCl solutions to describe the electromagnetic properties of the sea ice brine. However, when the model electromagnetic data for the 0.75-m-thick ice sheet are recalculated for 80 MHz (Table 4b), the center frequency at which the field data were taken, ϵ_a increases from 6.3 to 7 and fits nicely along the extrapolated line representing the field data as shown in Figure 22.

Along with the modeled physical properties, the electromagnetic properties of the nine ice sheets, as a function of depth increment, are also listed in Tables 1–9.

The V_m values for each ice sheet having been averaged to obtain V_a as previously discussed, V_a was plotted versus depth as shown in Figure 23. As with the ϵ_a versus ice thickness curve in Figure 21, statistically the power curve given in Figure 23 fits the data best. Nevertheless, the visual curve fit, also shown, is more representative of the data trend.

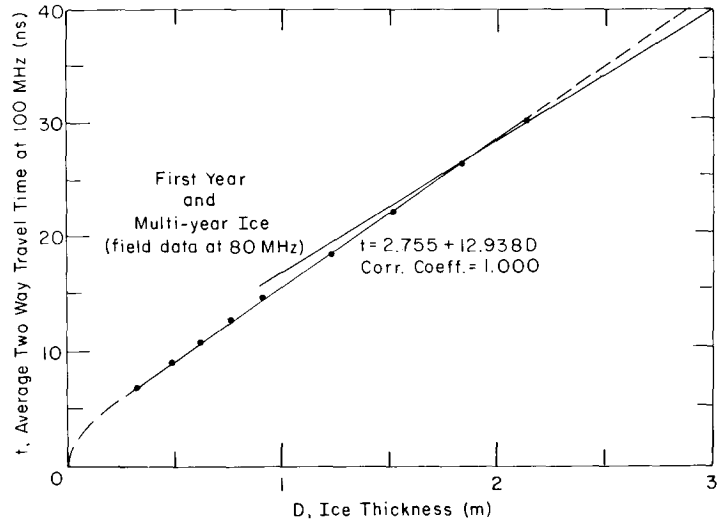

Figure 24. Average two-way travel time of 100-MHz wave in model sea ice versus ice sheet thickness.

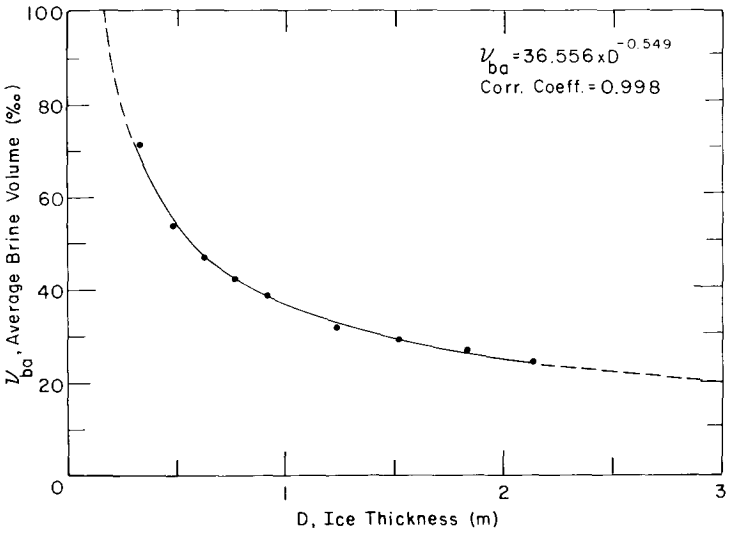

Figure 25. Average brine volume for model sea ice versus ice sheet thickness.

A related plot which would be extremely useful to a person using impulse radar to profile sea ice thickness is one giving the two-way flight time t of the electromagnetic wavelet in ice versus thickness, since this time is what is measured with these systems. A plot of t versus ice thickness was constructed using V_a and the ice sheet thickness in eq 21 to obtain t (Fig. 24). This curve is shown in relation to one developed for our 1985 first- and multi-year sea ice field data. The two curves provide similar results, less than 10% variation for ice 1 to 3 m thick. This implies that the plot for the model ice cover of t versus D may be used for estimating winter sea ice thickness using the two-way flight time information obtained with the use of impulse radar operating at a center frequency of about 100 MHz.

Other illustrative plots can be made with the data listed in Tables 1–9. For example, Figure 25 shows the average brine volume ν_{ba} for each ice sheet versus thickness. The data trend is as expected; as the ice thickens it becomes proportionately fresher due to brine drainage.

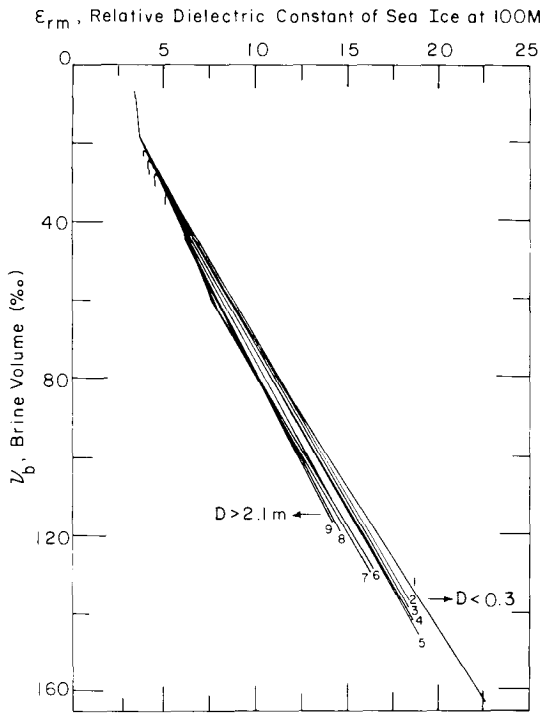

Figure 26. Relative dielectric constant of model sea ice at 100 MHz versus incremented ice sheet brine volume.

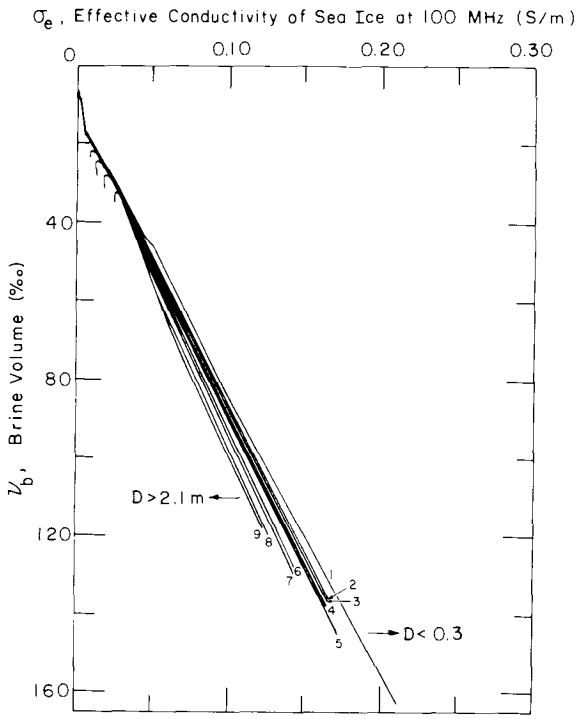

Figure 27. Effective conductivity of model sea ice at 100 MHz versus incremented ice sheet brine volume.

A plot of ϵ_{rm} versus brine volume ν_b for the nine model ice sheets (Fig. 26) shows that ϵ_{rm} is not uniquely related to ν_b. If a direct relation existed the plot would consist of a single curve. The variation in ϵ_{rm} versus ν_b for the different ice sheets is due to temperature effects. In short, at a given ice temperature it is possible to have different ice salinity concentrations and therefore different brine volumes within the ice sheet.

Similar curves are generated when the effective conductivity σ_e of each ice sheet is plotted versus ν_b (Fig. 27). The reason for the variation in the σ_e versus ν_b curves is given above. The higher volume of brine in the thinner ice increases the conductivity of the ice by providing for a proportionately larger concentration of free ions to react with the electromagnetic field.

The average effective conductivity σ_{ea} of the ice sheets versus thickness is presented in Figure 28. As with similar plots for ϵ_a and ν_{ba}, σ_{ea} is shown to decrease, as expected, with increased ice sheet thickness. This trend for σ_{ea} is due to a decrease in ν_{ba}, the number of free ions available in the brine, and a lower brine ionic mobility in the thicker, colder ice. The relation between σ_{ea} and ν_{ba} is shown in Figure 29 with ice thickness as a parameter. Again, the thinner winter model ice sheet has the highest σ_{ea}.

Since there are devices available to measure σ_{ea}, it would appear that, through the relationships shown in Figures 28 and 29, both the thickness and average brine volume of the ice could be determined. We are currently pursuing studies in this area. In addition, since certain sea ice mechanical properties are governed by brine volume, for example the elastic modulus and flexural strength as shown in Figures 30 and 31, it would appear that by remotely estimating this volume an assessment of the ice cover strength could be made.

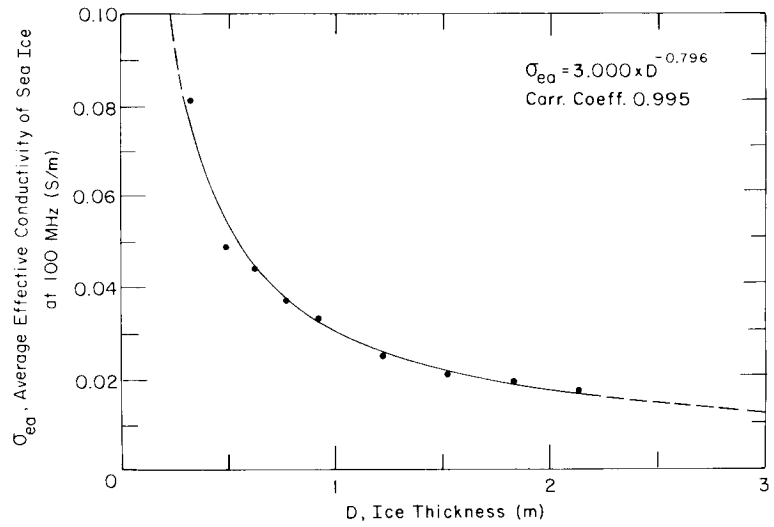

Figure 28. Average effective conductivity of model sea ice at 100 MHz versus ice sheet thickness.

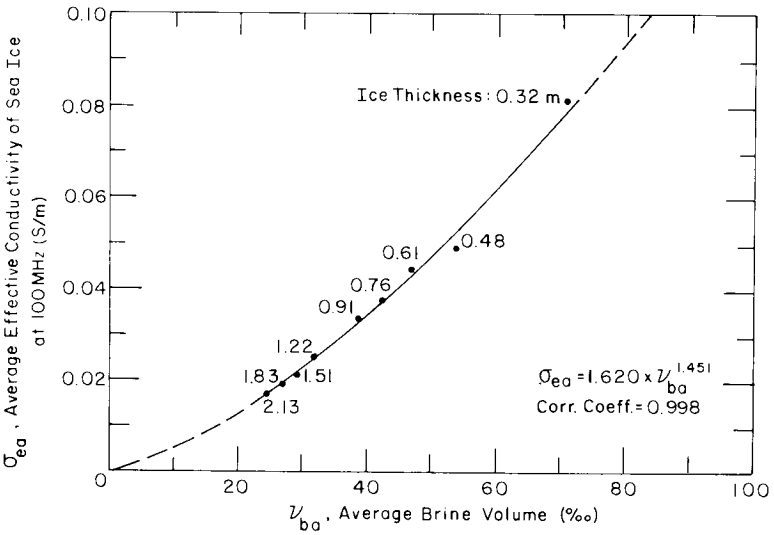

Figure 29. Average effective conductivity of model sea ice at 100 MHz versus average ice sheet brine volume with ice sheet thickness as a parameter.

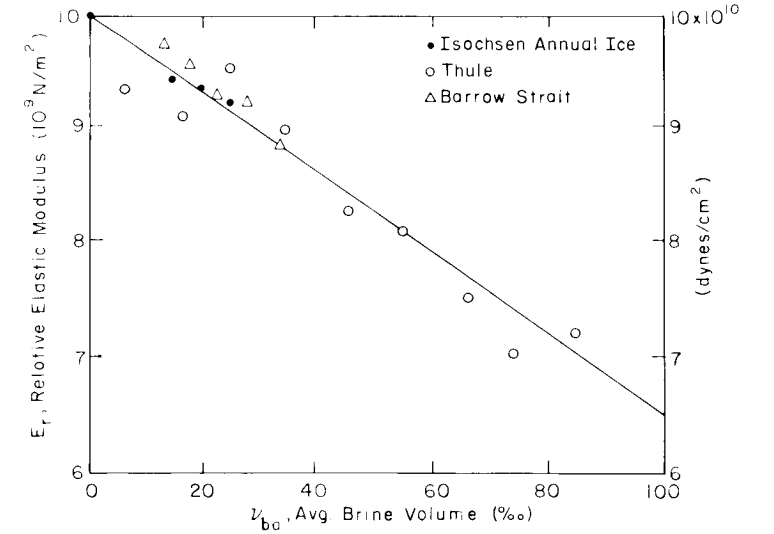

Figure 30. Relative elastic modulus of small sea ice test samples versus average brine volume (after Cox and Weeks 1985).

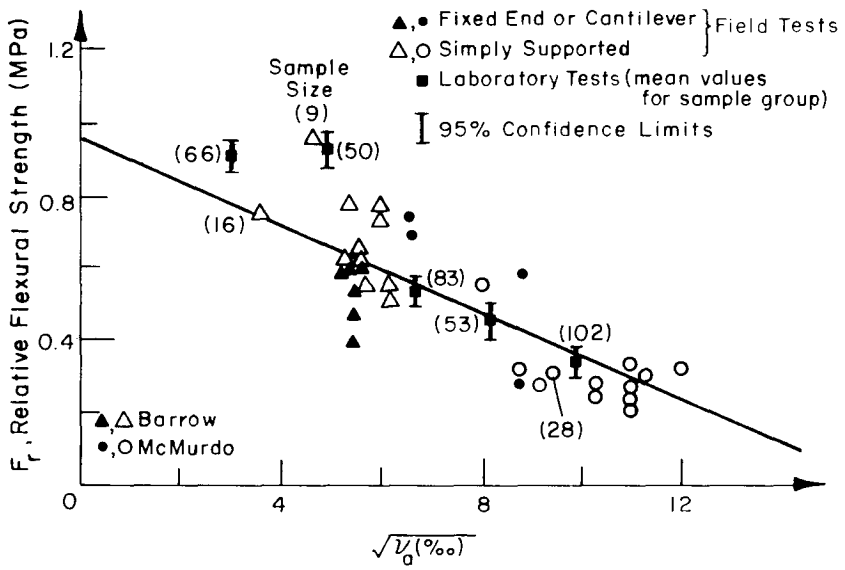

Figure 31. Relative flexural strength of sea ice versus square root of the average brine volume of the ice (after Cox and Weeks 1985).

Electromagnetic properties of model sea ice at 100 and 500 MHz and 1 and 5 GHz

The electromagnetic properties of first-year sea ice versus depth at a frequency of 100 MHz have been discussed. This section will give modeled electromagnetic property results at 500 MHz, 1 GHz and 5 GHz for the 0.76-m-thick model 4 ice sheet, and compare these new properties with those previously determined at 100 MHz. The same analyses as previously discussed were used for calculating the electromagnetic data for the ice at the new frequencies. The physical and electromagnetic properties of the ice are listed versus depth in Tables 10–12. Ice temperature, salinity, brine volume and brine-free ice density, and the brine conductivity versus depth in the 0.76-m-thick ice sheet, are shown in Figures 32–36. The relative real (ϵ'_{rb}) and imaginary (ϵ''_{rb}) parts of the complex dielectric constant of the brine are presented in Figures 37 and 38. Between 100 MHz and 1 GHz, ϵ'_{rb} remains relatively unchanged.

Table 10. Physical and electromagnetic properties of 0.76-m-thick model ice sheet 4 using NaCl brine conductivities at 500 MHz.

Depth		Ice	Ice	Bulk	Brine	Ice	σ_{DCb}	ϵ'_{rb}	ϵ''_{rb}	σ_{DCI}	σ_e	A	ϵ_{rm}	ϵ'_{rm}	ϵ''_{rm}
Depth cm	Incr cm	temp -°C	sal ‰	den_3 Mg/m	vol ‰	den_3 Mg/m	S/m			S/m	S/m	dB/m			
2.5	0-05	21.1	8.7	.928	28.3	.894	3.48	29.42	126.62	.012	.017	14.48	3.83	3.81	.178
7.5	5-10	19.8	7.5	.927	25.5	.896	3.82	32.80	138.93	.012	.016	13.18	3.77	3.75	.148
12.5	10-15	18.5	6.9	.926	24.6	.897	4.17	35.85	151.80	.012	.016	13.15	3.76	3.74	.133
17.5	15-20	17.2	6.5	.926	24.4	.897	4.53	38.63	164.84	.013	.016	13.63	3.76	3.74	.123
22.5	20-25	15.8	6.3	.925	25.1	.896	4.91	41.35	178.66	.014	.018	15.62	3.76	3.72	.116
27.5	25-30	14.5	6.1	.925	25.8	.895	5.25	43.66	190.91	.016	.019	16.18	3.81	3.76	.114
32.5	30-35	13.2	6.0	.925	27.1	.894	5.56	45.79	202.28	.018	.022	18.03	3.85	3.81	.113
37.5	35-40	11.9	5.9	.925	28.7	.892	5.84	47.79	212.51	.021	.024	20.25	3.89	3.84	.114
42.5	40-45	10.5	5.8	.925	31.0	.890	6.10	49.82	221.94	.025	.028	23.29	3.96	3.90	.118
47.5	45-50	9.2	5.8	.925	34.4	.887	6.30	51.61	229.02	.030	.034	27.60	4.07	3.98	.126
52.5	50-55	7.9	5.8	.925	38.9	.882	6.32	54.21	229.89	.037	.041	32.80	4.20	4.07	.140
57.5	55-60	6.6	5.8	.926	45.2	.876	5.98	58.40	217.91	.045	.049	38.48	4.37	4.20	.165
62.5	60-65	5.2	5.8	.926	55.8	.866	5.41	63.04	197.86	.056	.062	47.06	4.67	4.40	.209
67.5	65-70	3.9	6.2	.928	78.1	.846	4.58	67.64	171.76	.083	.091	64.71	5.32	4.82	.299
72.5	70-75	2.6	7.5	.934	141.6	.787	3.71	72.66	137.37	.168	.182	110.58	7.30	5.82	.507

Table 11. Physical and electromagnetic properties of 0.76-m-thick model ice sheet 4 using NaCl brine conductivities at 1 GHz.

Depth		Ice	Ice	Bulk	Brine	Ice	σ_{DCb}	ϵ'_{rb}	ϵ''_{rb}	σ_{DCi}	σ_e	A	ϵ_{rm}	ϵ'_{rm}	ϵ''_{rm}
Depth cm	Incr cm	temp -°C	sal ‰	den_3 Mg/m^3	vol ‰	den_3 Mg/m^3	S/m			S/m	S/m	dB/m			
2.5	0-05	21.1	8.7	.928	28.3	.894	3.48	29.13	65.55	.012	.025	21.70	3.70	3.68	.236
7.5	5-10	19.8	7.5	.927	25.5	.896	3.82	32.48	71.98	.012	.023	19.38	3.66	3.65	.200
12.5	10-15	18.5	6.9	.926	24.6	.897	4.17	35.52	78.65	.012	.022	18.86	3.66	3.65	.183
17.5	15-20	17.2	6.5	.926	24.4	.897	4.53	38.27	85.38	.013	.022	19.07	3.67	3.66	.172
22.5	20-25	15.8	6.3	.925	25.1	.896	4.91	40.97	92.49	.014	.024	20.26	3.69	3.68	.168
27.5	25-30	14.5	6.1	.925	25.8	.895	5.25	43.26	98.78	.016	.025	21.49	3.71	3.70	.165
32.5	30-35	13.2	6.0	.925	27.1	.894	5.56	45.39	104.62	.018	.028	23.43	3.75	3.73	.166
37.5	35-40	11.9	5.9	.925	28.7	.892	5.84	47.38	109.86	.021	.031	25.78	3.79	3.77	.169
42.5	40-45	10.5	5.8	.925	31.0	.890	6.10	49.40	114.71	.025	.035	29.10	3.85	3.82	.176
47.5	45-50	9.2	5.8	.925	34.4	.887	6.30	51.18	118.35	.030	.041	33.90	3.93	3.89	.190
52.5	50-55	7.9	5.8	.925	38.9	.882	6.32	53.76	118.99	.037	.049	39.74	4.02	3.98	.207
57.5	55-60	6.6	5.8	.926	45.2	.876	5.98	57.89	113.41	.045	.058	46.27	4.15	4.08	.233
62.5	60-65	5.2	5.8	.926	55.8	.866	5.41	62.48	103.82	.056	.072	56.21	4.35	4.26	.276
67.5	65-70	3.9	6.2	.928	78.1	.846	4.58	67.03	91.17	.083	.103	76.82	4.79	4.61	.357
72.5	70-75	2.6	7.5	.934	141.6	.787	3.71	72.01	74.38	.168	.197	131.67	6.03	5.50	.522

Table 12. Physical and electromagnetic properties of 0.76-m-thick model ice sheet 4 using NaCl brine conductivities at 5 GHz.

Depth		Ice	Ice	Bulk	Brine	Ice	σ_{DCb}	ϵ'_{rb}	ϵ''_{rb}	σ_{DCi}	σ_e	A	ϵ_{rm}	ϵ'_{rm}	ϵ''_{rm}
Depth cm	Incr cm	temp -°C	sal ‰	den_3 Mg/m^3	vol ‰	den_3 Mg/m^3	S/m			S/m	S/m	dB/m			
2.5	0-05	21.1	8.7	.928	28.3	.894	3.48	22.62	23.38	.012	.069	61.05	3.45	3.45	.205
7.5	5-10	19.8	7.5	.927	25.5	.896	3.82	25.24	26.02	.012	.062	54.78	3.44	3.44	.182
12.5	10-15	18.5	6.9	.926	24.6	.897	4.17	27.65	28.57	.012	.060	52.86	3.46	3.46	.173
17.5	15-20	17.2	6.5	.926	24.4	.897	4.53	29.85	31.00	.013	.060	52.55	3.48	3.47	.169
22.5	20-25	15.8	6.3	.925	25.1	.896	4.91	32.04	33.48	.014	.062	54.30	3.50	3.50	.171
27.5	25-30	14.5	6.1	.925	25.8	.895	5.25	33.91	35.62	.016	.064	56.07	3.52	3.52	.173
32.5	30-35	13.2	6.0	.925	27.1	.894	5.56	35.67	37.59	.018	.068	59.23	3.55	3.55	.179
37.5	35-40	11.9	5.9	.925	28.7	.892	5.84	37.35	39.37	.021	.073	63.00	3.58	3.58	.185
42.5	40-45	10.5	5.8	.925	31.0	.890	6.10	39.08	41.06	.025	.080	68.41	3.63	3.62	.196
47.5	45-50	9.2	5.8	.925	34.4	.887	6.30	40.65	42.41	.030	.090	76.38	3.68	3.68	.212
52.5	50-55	7.9	5.8	.925	38.9	.882	6.32	42.68	43.56	.037	.101	85.62	3.75	3.75	.231
57.5	55-60	6.6	5.8	.926	45.2	.876	5.98	45.61	44.29	.045	.115	95.56	3.86	3.84	.252
62.5	60-65	5.2	5.8	.926	55.8	.866	5.41	48.93	44.38	.056	.136	110.96	4.02	4.00	.286
67.5	65-70	3.9	6.2	.928	78.1	.846	4.58	52.34	43.76	.083	.183	143.37	4.36	4.33	.359
72.5	70-75	2.6	7.5	.934	141.6	.787	3.71	56.25	42.40	.168	.316	226.04	5.23	5.17	.530

However, there is a marked decrease in ϵ'_{rb} at 5 GHz as a result of dipole water relaxation processes. ϵ''_{rb} is seen to increase gradually from 5 GHz to 500 MHz, but then undergoes a large increase at 100 MHz. This variation is due to conductivity effects, as can be inferred from Figure 39, which gives the relative real (ϵ'_{rb}) and imaginary (ϵ''_{rb}) dielectric constants of the brine at -10.5 °C versus frequency. Below about 10^8 Hz the second term ($\sigma_{DCb}/\omega\epsilon_o$) of ϵ''_{rb} in eq 10 dominates and is inversely proportional to frequency. For this reason ϵ''_{rb} increases exponentially below about 10^{10} Hz. Above about 10^8 Hz, the first term of ϵ''_{rb} in eq 10 dominates.

The variation of the relative real (ϵ'_{rm}) and imaginary (ϵ''_{rm}) parts of the complex dielectric constant of sea ice versus depth at the four frequencies is given in Figures 40 and 41. ϵ'_{rm} and ϵ''_{rm} are seen to increase with depth following the increase in brine volume (Fig. 34). The large increase in ϵ''_{rm} from 100 MHz to 500 MHz and 1 GHz clearly indicates the ice is more lossy at these frequencies. This is also shown to occur in the plot of attenuation A versus depth in Figure 42. As expected, the largest increase in A occurs at 5 GHz. Since the complex dielectric constant ϵ_i^* for pure ice is constant from about 10^5 Hz to above 10^{12} Hz (Fig. 43), the

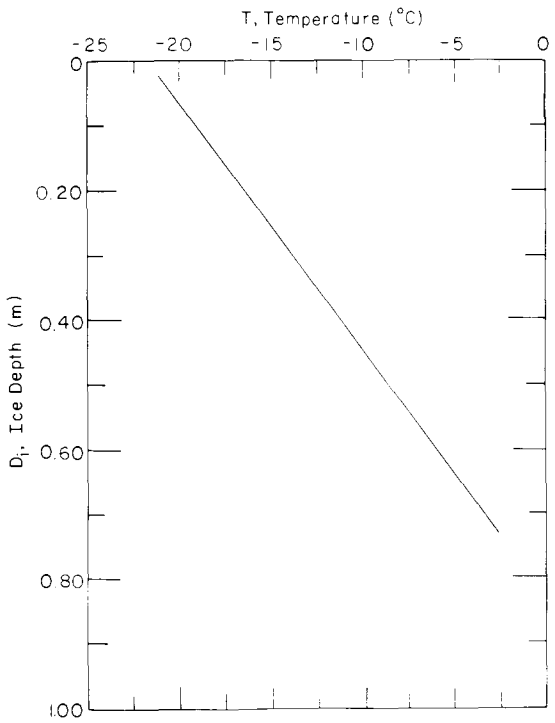

Figure 32. Model ice sheet temperature versus depth.

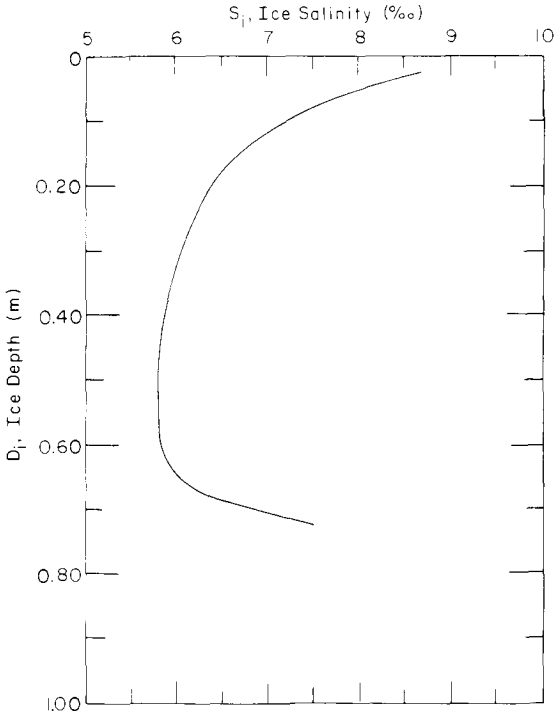

Figure 33. Model ice sheet salinity versus depth.

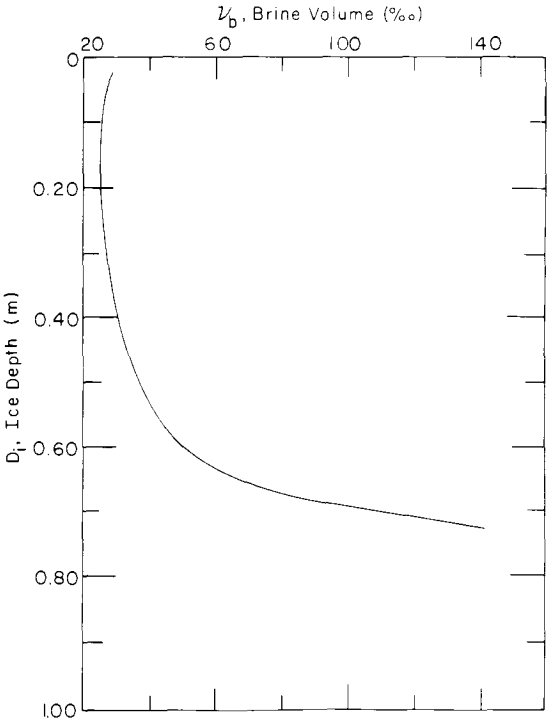

Figure 34. Model ice sheet brine volume versus depth.

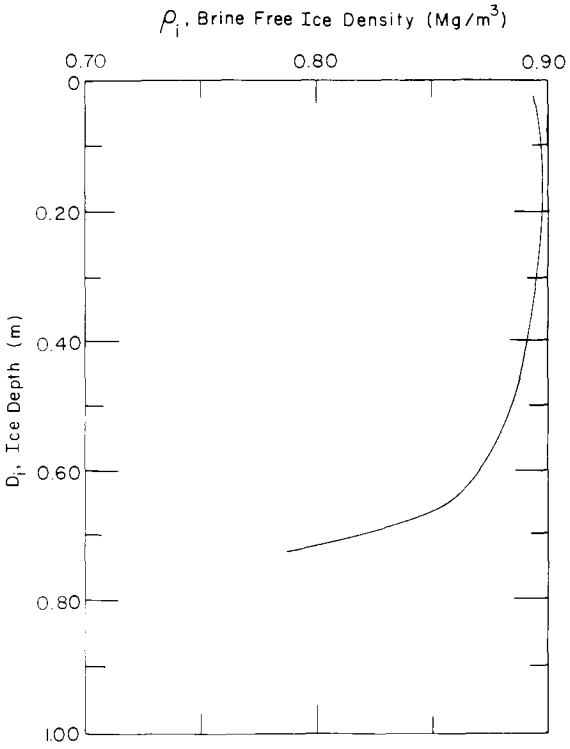

Figure 35. Model ice sheet brine-free ice density versus depth.

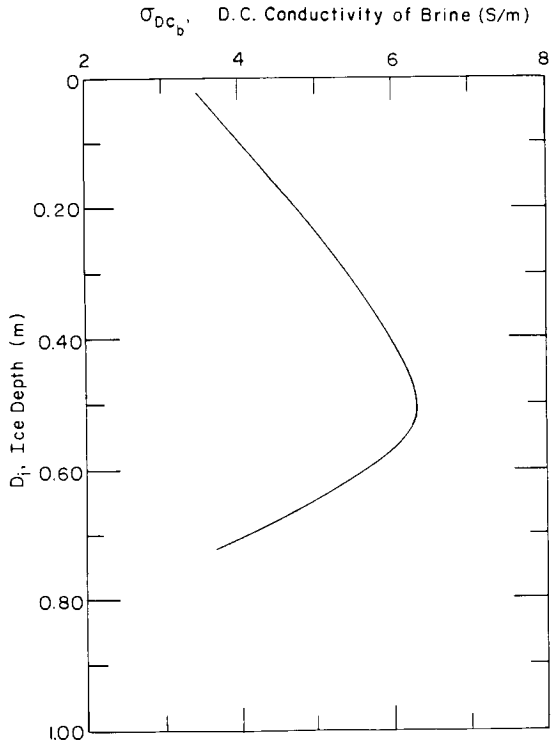

Figure 36. DC conductivity of model brine versus ice sheet depth.

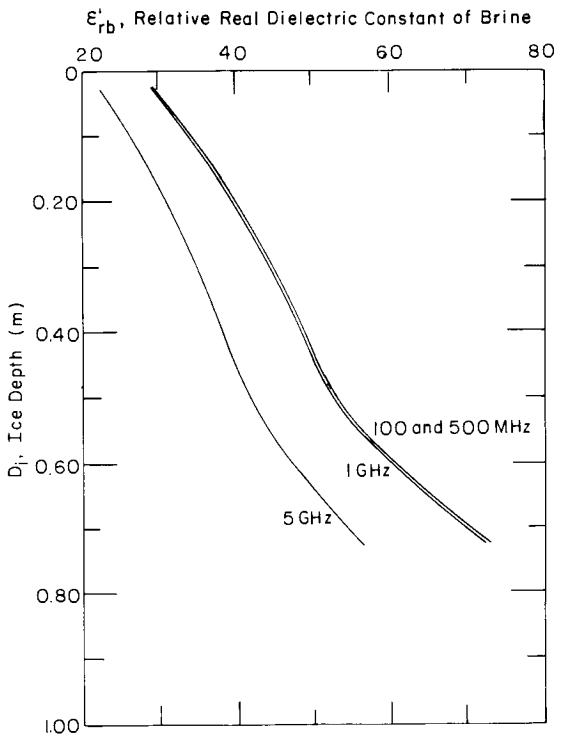

Figure 37. Relative real dielectric constant of model brine versus ice sheet depth with frequency as a parameter.

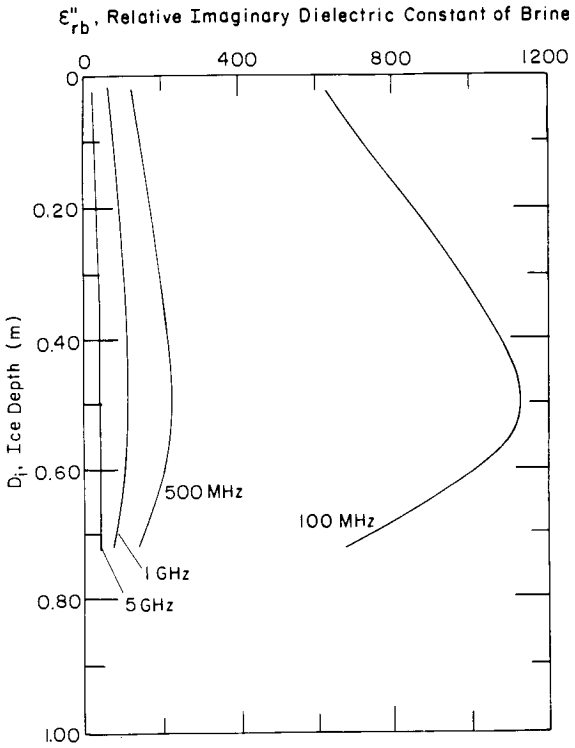

Figure 38. Relative imaginary dielectric constant of model brine versus ice sheet depth with frequency as a parameter.

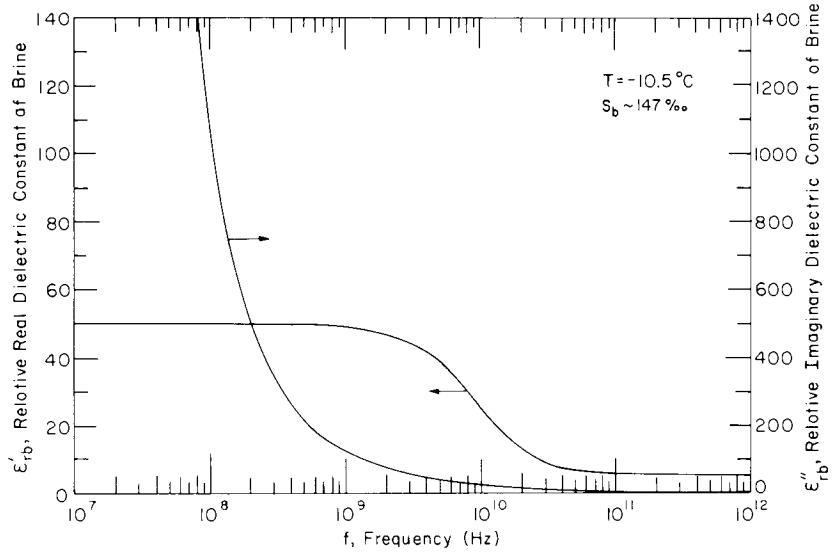

Figure 39. Relative complex dielectric constant of model brine versus frequency.

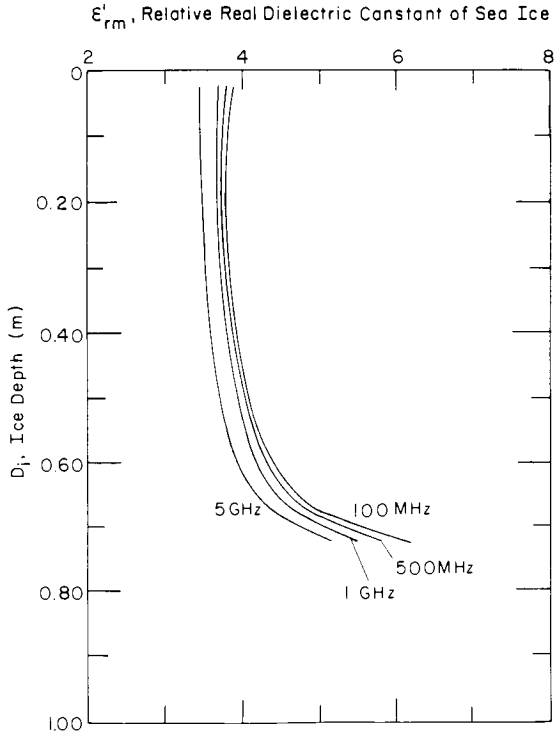

Figure 40. Relative real dielectric constant of model sea ice versus ice depth with frequency as a parameter.

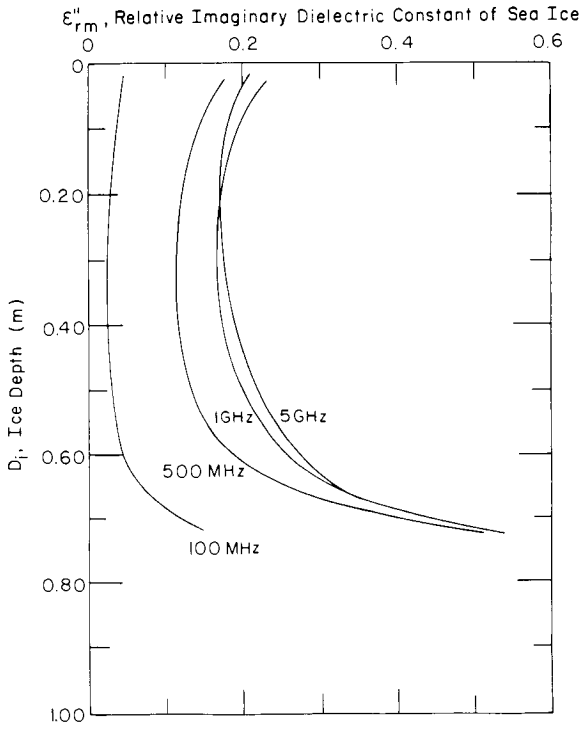

Figure 41. Relative imaginary dielectric constant of model sea ice versus ice depth with frequency as a parameter.

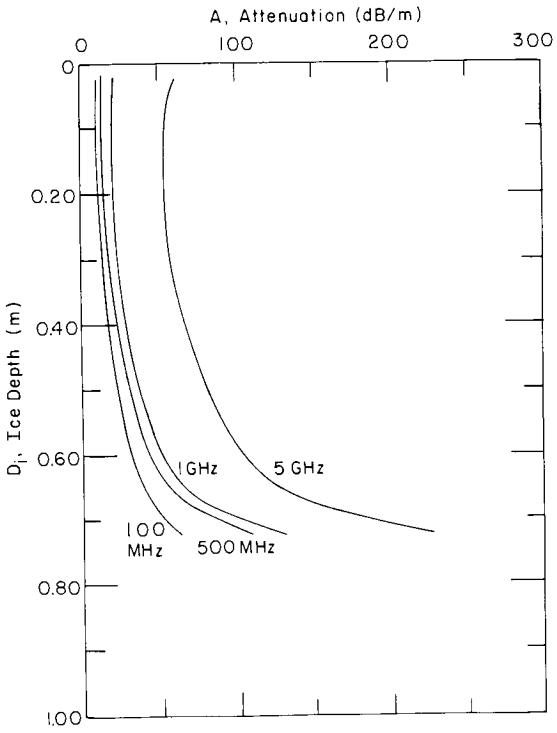

Figure 42. Attenuation in model sea ice versus depth with frequency as a parameter.

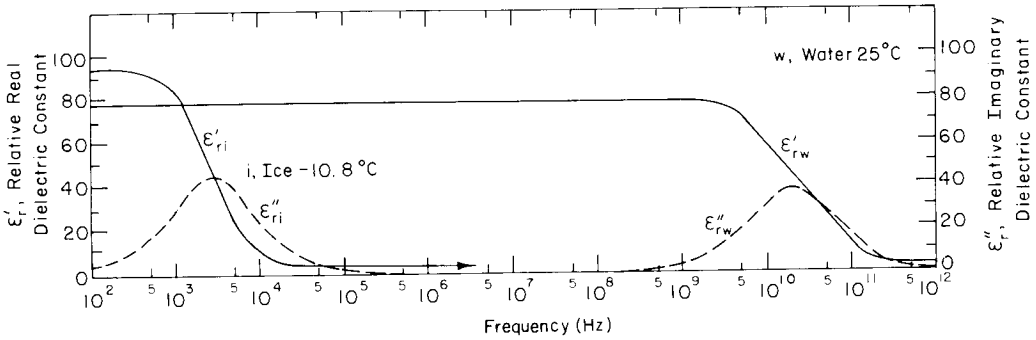

Figure 43. Relative complex dielectric constants of pure water (σ_{DC} = 0) and freshwater ice versus frequency (after Hoekstra and Doyle 1971).

changes in the electromagnetic properties of the brine with frequency thus dominate the above noted changes. For example, ϵ'_{rb} for the model brine at -10.5 °C decreases from about 50 around 10^8 Hz to about 5.5 near 10^{11} Hz (Fig. 39). Therefore, ϵ'_{rm} should decrease with increasing frequency as illustrated in Figure 40.

The frequency-dependent complex dielectric constant of the model sea ice is illustrated in Figure 44 for the ice properties listed. ϵ'_{rm} is shown to decrease "step-wise" between about 10^8 Hz and 10^{11} Hz, while ϵ''_{rm} increases "step-wise" from about 10^7 Hz to 2×10^{10} Hz, whereupon it begins to decrease. The steps in the curves between about 2×10^{10} and 5×10^9 Hz are due to the $\sigma_{DCb}/\omega\epsilon_o$ term of ϵ''_{rb} in eq 10, which is used to calculate ϵ^*_{rb}, which in turn is used to determine ϵ'_{rm} and ϵ''_{rm} in eq 17. The change that is centered at about 2.5×10^{10} Hz is due to the Debye relaxation process.

The plot of ϵ_{rm} versus depth in Figure 45 is interesting for it shows a marked decrease in ϵ_{rm} between 100 MHz and 500 MHz, especially in the lower half of the ice sheet. This change is again directly related to the frequency-dependent electromagnetic properties of the brine, as previously discussed.

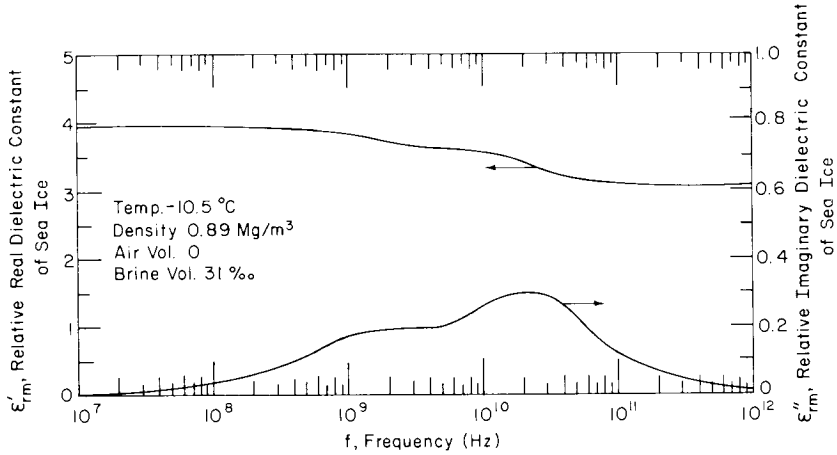

Figure 44. Relative complex dielectric constant of model sea ice versus frequency.

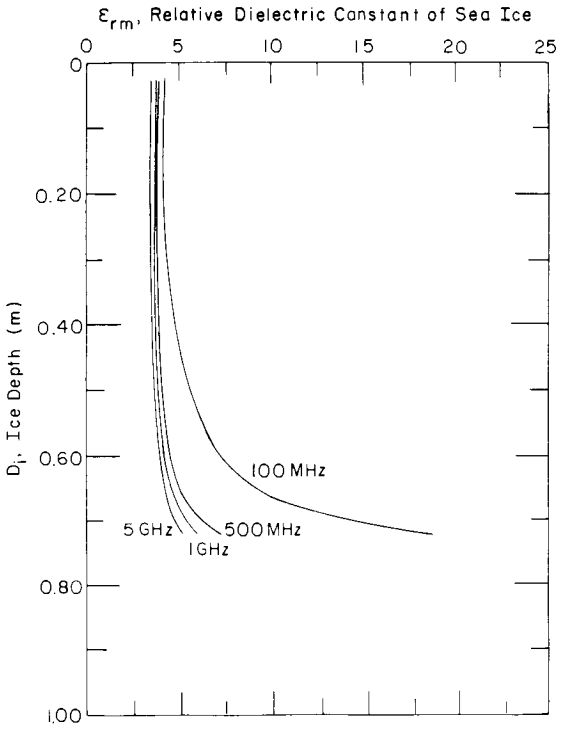

Figure 45. Relative dielectric constant of model sea ice versus depth with frequency as a parameter.

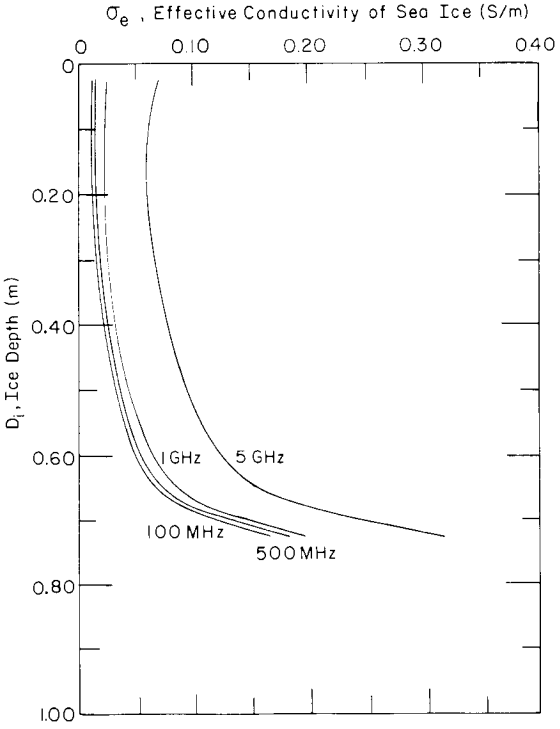

Figure 46. Effective conductivity of model sea ice versus depth with frequency as a parameter.

The effective conductivity σ_e of the sea ice versus depth is presented in Figure 46. The trend is as expected in that σ_e increases with depth following the trend of ν_b versus depth shown in Figure 34.

Part II of this report series will show the effect of using equations 3-9, instead of expressions for true sea ice brine, in the determination of the relative EM properties of sea ice. It will be shown that the EM property trends versus depth presented here are representative of those created using the electrical properties of natural sea water brine.

Example of impulse radar sea ice profiling results

The impulse radar system used in our field studies to profile sea ice thickness consisted of timing electronics which clock a pulse generator and sampling head. The pulse source gener-

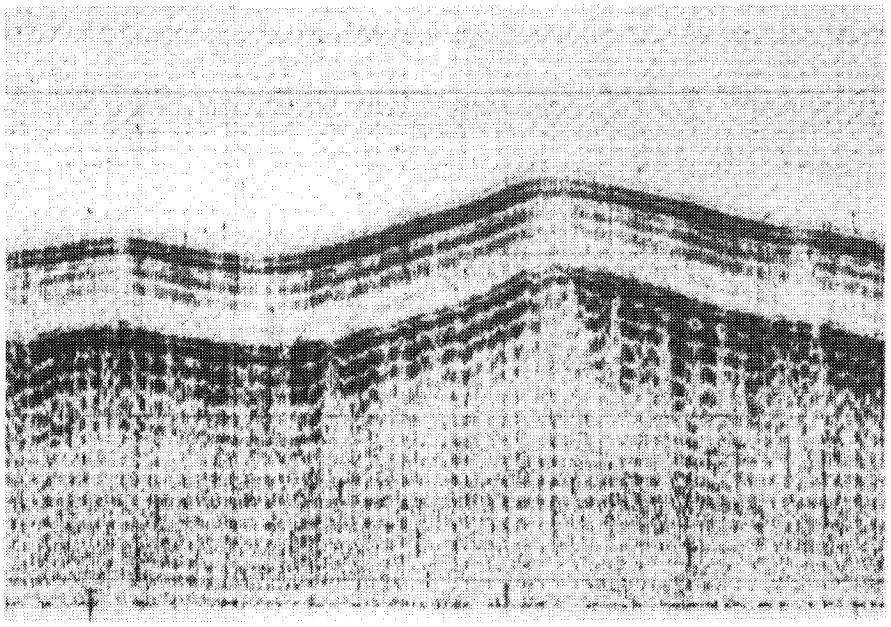

Figure 47. Graphic record of airborne impulse radar echo sounding of 1¾-m-thick first-year sea ice. The long period variation in the record is due to changing helicopter altitude. Record length represents about ½ km of flight line. (From Kovacs and Morey, 1980.)

ates pulses with a 3-dB bandwidth on the order of 200 MHz at a repetition rate of 50 kHz and a pulse width of 1 to 5 ns. The pulse is fed to a transmitting/receiving antenna which radiates an electromagnetic wavelet into the underlying material. Typical antennas used have free space transmitted wavelet spectrum center frequencies of about 80, 120 and 300 MHz.

The transmitted wavelet travels from the transmit antenna to the surface and into the target. The wavelet energy that is not scattered or absorbed is reflected back to the receiver antenna from the surface and various interfaces within the medium being sounded. The received signal is then displayed on a graphic recorder, similar to the way information is recorded from an acoustic sub-sea-bottom profiling system. The graphic record is a display of the travel time of the wave to various reflecting interfaces and back to the receiver antenna, or the two-way travel time of the wavelet. The depth of penetration and the propagation velocity of the wavelet in sea ice are functions of the electromagnetic properties of the component parts and their interrelationship as previously discussed.

To convert the two-way travel time (as displayed on the graphic record) to depth, it is necessary to know the apparent propagation velocity V_a of the wavelet within the intervening medium. Depth can then be estimated from eq 21. V_a is a function of the apparent dielectric constant ϵ_a of the medium. This value is generally unknown. However, it is now possible to estimate sea ice thickness using the two-way wavelet flight time in the equation given in Figure 24 or with the aid of Figure 21 and eq 21 and 22.

We have been successful in profiling cold winter undeformed first-year sea ice from the surface and from a low-flying helicopter as shown in Figure 47 (Kovacs and Morey 1980), but not "warm" sea ice or sea ice with high brine content. This sounding inability stems from reasons previously discussed in the model results and is predominantly caused by high losses associated with high brine volume and related ice conductivity. Deformed sea ice cannot be profiled because of the presence of highly conductive seawater within the submerged ice rubble. The impulse radar antenna has been hard-mounted to the helicopter on brackets extending out from the aircraft structure or carried in a sling. Both methods are shown in Figure 48.

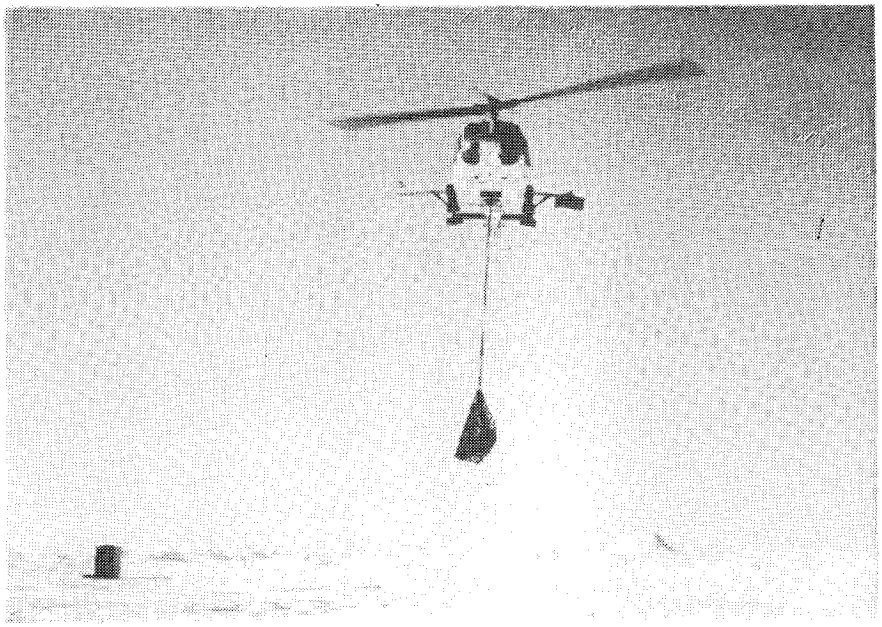

Figure 48. Example of hard-mounted and slung impulse radar antennas on helicopter. The tilted dark object in the net is an antenna which is turned horizontal when in use.

Profiling multi-year sea ice has met with mixed results. For example, the cross section of a multi-year ridge determined using elevation survey and drill hole measurements is given in Figure 49a. An impulse radar profile was run over the ridge by dragging the radar antenna on the surface. The graphic profile record obtained is given in Figure 49b. A depth scale for the profile was created by assuming that this thick ice had an apparent dielectric constant of 3.4, as may be inferred from Figure 22, and thus an effective velocity of 0.163 m/ns. Using this velocity, the time scale for the record (not shown) was converted to the depth scale shown. The white dots on the graphic record represent the measured drill hole depths, and the first white band (first plus to minus voltage zero crossing of the reflected wavelet energy) represents the bottom interface. As this record shows, the agreement betwen the indirect radar determination and the measured ice thickness is quite good.

For another ridge (Fig. 50a), where the bottom of the keel was found to consist of moist, and in some places rather "wet," ice, the above agreement did not hold. The radar profile along this ridge is given in Figure 50b. The white dots represent the drill-hole-measured ice thicknesses, and the dashed white line represents the apparent ice bottom. There is reasonable agreement between the drill hole measurements and the radar bottom interface only at stations 3, 4 and 17–20. The black dots represent the relative depth to the moist zone as determined from the consistency of the cuttings removed during drilling. This method of determining the depth to the moist interface is not very accurate because the boundary is not necessarily a sharp one and the cuttings take time to appear at the surface. The depth from which the cuttings originated could only be estimated. Nevertheless, the data indicate that between stations 4 and 7 the interface profiled by the radar was not the ice bottom but the top of the moist zone. This also indicates that in this ridge there was a good dielectric contrast at the "dry" and "wet" ice boundary, which provided a good reflective interface. This is evident between stations 11 and 16, where the intensity (amplitude) of the reflected EM wavelet, as indicated by the darkness of the record, was quite high. If the boundary was not well defined or was diffused, the EM wavelet energy could be absorbed, with no reflection seen in the record. This condition has been encountered and thus complicates data interpre-

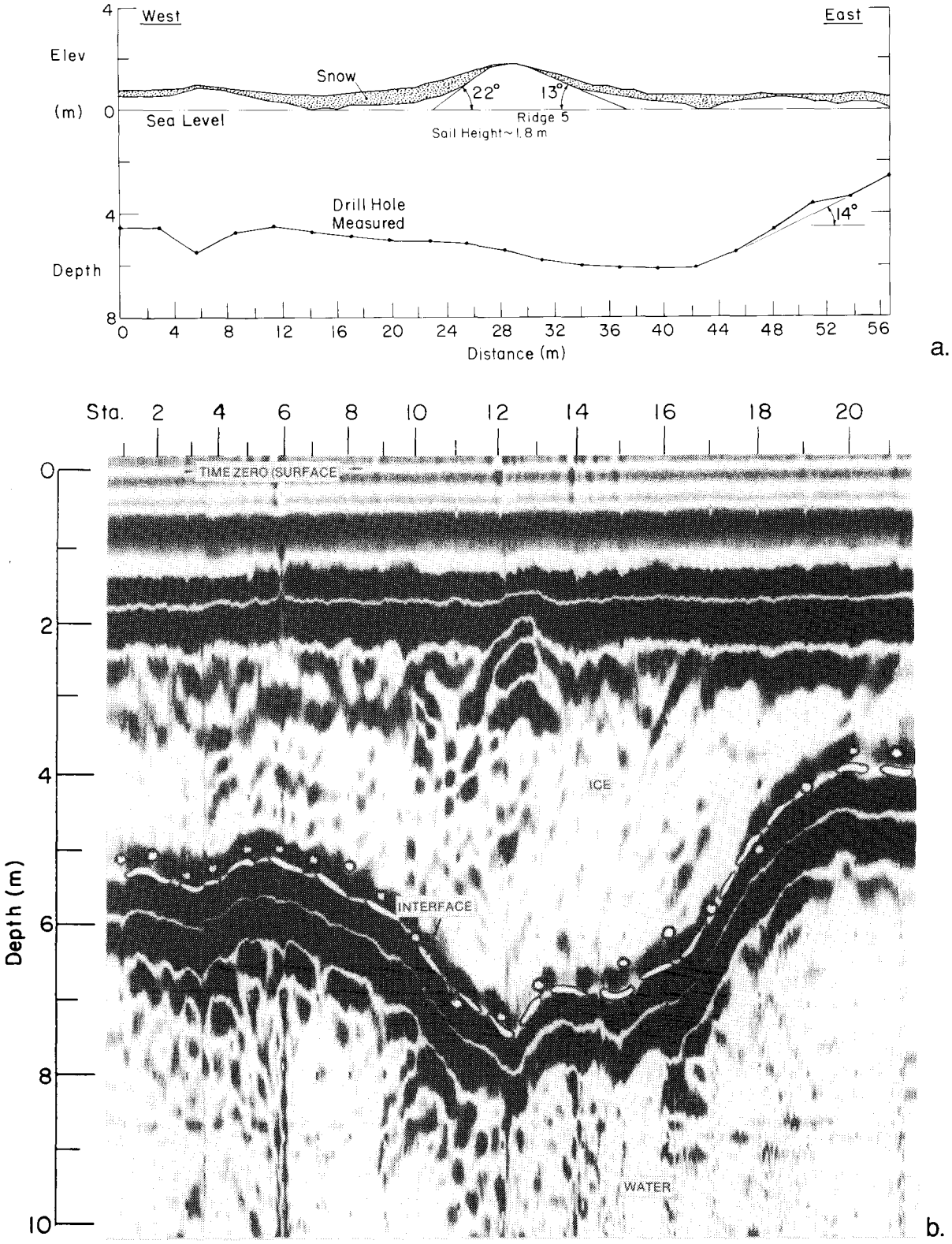

Figure 49. Cross section of ridge 5 as determined by drill hole measurement and elevation survey (a), and graphic record of impulse radar profile of ridge 5 obtained by dragging an 80-MHz antenna along the surface (b). (From Kovacs and Morey 1986.)

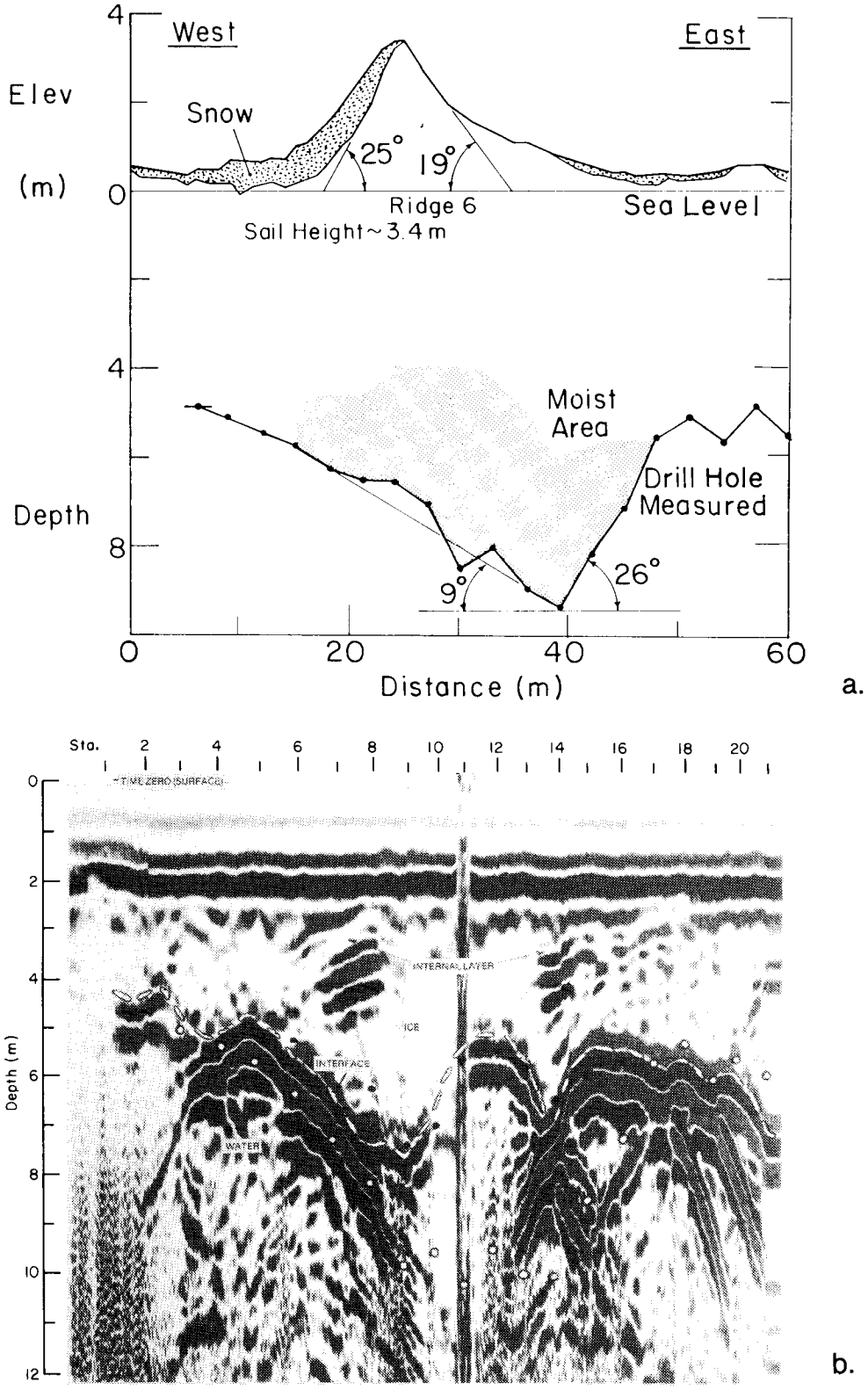

Figure 50. Cross section of ridge 6 as determined by drill hole measurement and elevation survey (a), and graphic record of impulse radar profile of ridge 6 obtained by dragging an 80-MHz antenna along the surface (b). (From Kovacs and Morey 1986.)

tation and reduces the usefulness of impulse radar sounding of sea ice. In short, there are conditions where no return from a subsurface interface is obtained due to absorption and scattering losses, and where the return is from an interface well above the ice/water boundary, such as the top of a conductive wet zone in the ice. Further information on our impulse radar measurements on first- and multi-year sea ice can be found in Kovacs and Morey (1980, 1986) and Kovacs et al. (1981).

Example of frequency-domain electromagnetic sea ice thickness sounding

At frequencies below a few hundred kilohertz, the form of the complex propagation constant given in eq 11 simplifies to

$$\gamma = \sqrt{j\omega\mu_0\sigma_e}$$

This has major implications for the nature of EM propagation in conductors such as ice and seawater. In particular, the electromagnetic fields are governed by a diffusion equation rather than a wave equation. The result is that energy reflected from the ice and water surfaces is not seen as temporally compact reflection events at the receiver, but rather is spread out over a wide time window. Special techniques must therefore be used to acquire and process such data. An airborne electromagnetic (AEM) measurement system is designed to perform this task.

An airborne electromagnetic (AEM) system was used for the first time in May 1985 for the purpose of estimating sea ice thickness, water conductivity, and water depths from about 1 to 20 m under the ice cover. The AEM system was basically a standard geophysical exploration device used by industry for airborne detection of highly conductive mineral deposits. The concept of using this technology for measuring coastal bathymetry was recently reviewed by Morrison and Becker (1982) and for determining sea ice thickness by Becker et al. (1983). The feasibility of using AEM techniques for measuring sea ice thickness perhaps originated in 1968 (Anon.) but was not pursued beyond an analytical verification. The AEM system used in our field study had four pairs of antenna coils (transmit Tx and receive Rx). The coils allowed simultaneous operation at nominal frequencies of 530, 930, 4158 and 16,290 Hz. A fifth frequency of 32,020 Hz was also evaluated by replacing the 16,290-Hz coils. The transmit-receive coils were separated about 6½ m inside a Kevlar tube (bird) 7½ m long and ½ m in diameter. The bird weighed about 200 kg, and was typically flown about 30 m above the ice surface (Fig. 51). In principle, the transmit coil produces a primary magnetic field H_p which causes a secondary magnetic field H_s when there is a conductive medium (e.g. seawater) below the bird. This is illustrated in Figure 52.

The primary and secondary magnetic fields are sensed by the receiver coils. The distance to and conductivity of the conductor affect the coefficient of mutual inductance or mutual coupling ratio H_s/H_p. Through the use of bucking coils and electronics, the primary field at the receiver is canceled out, and highly precise measurements of the in-phase (*IP*) and quadrature phase (*Q*) components of the secondary magnetic field, in parts per million (ppm), are made and recorded. With the aid of an Argand diagram, formulated on the basis of a given Tx and Rx coil spacing and orientation, the apparent conductivity and height of the bird above the conductive surface can be estimated. An example of an Argand diagram is given in Figure 53. If *IP* is 2000 ppm and *Q* is 850 ppm then the intercept of the related lines on the diagram indicates the bird is about 26 m above the conductor, or in our case the seawater, and the response parameter (frequency × conductivity) is 5000. In addition, if the coil was operating at a frequency of 2000 Hz, then the conductivity of the seawater would be 2.5 S/m (5000/2000 = 2.5). Through appropriate multilayer analyses, the Argand diagram can be refined and extended by nonlinear regression techniques to provide improved estimates of the

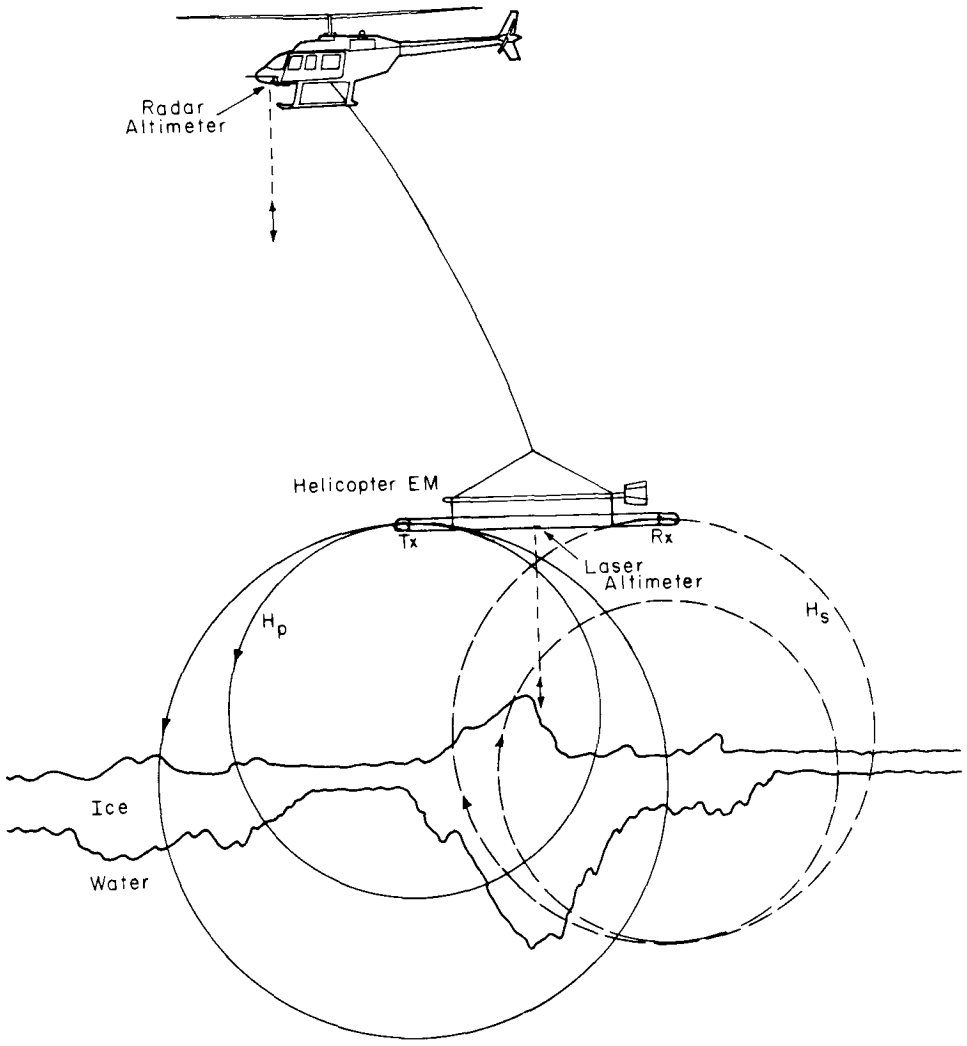

Figure 51. Illustration of helicopter-borne electromagnetic sensing system. The transmit coil creates a primary magnetic field H_p which sets up eddy currents in a conductive medium. A secondary magnetic field H_s thus results which is detected by the receive coil.

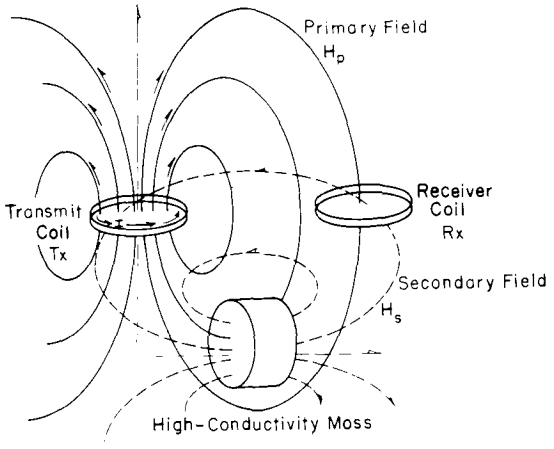

Figure 52. Illustration of the magnetic fields associated with AEM sensing using a horizontal coplanar (whale tail) coil arrangement. Other possible coil arrangements include vertical coplanar and vertical coaxial coils.

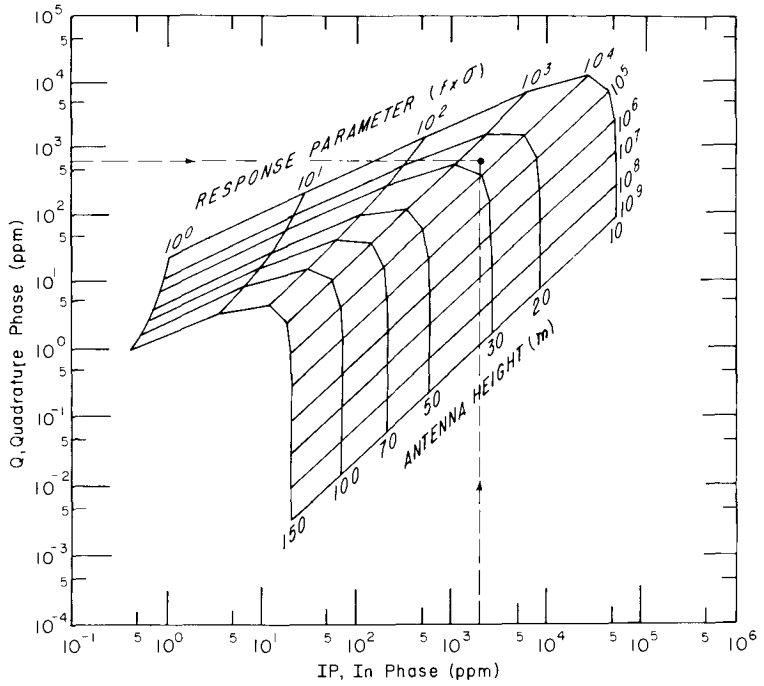

Figure 53. Example Argand diagram used for determining AEM bird elevation above (and the apparent conductivity of) a high-conductivity layer. The diagram models the response of a horizontal coplanar coil pair, separated about 6.5 m, above a halfspace.

properties of the sea ice and water and the seabed. A more detailed discussion of the theory used in our AEM sounding of sea ice and water can be found in Kovacs et al. (1987).

It is important to note that sea ice is relatively resistive at the AEM system's low frequencies, and therefore the ice is transparent. Since the AEM system determines the distance from the bird to the sea surface, the sea ice thickness needs to be determined with the use of a laser profilometer system. A laser was built into the bird, and used to measure the distance from the bird to the ice surface. Subtracting this distance from that determined by the AEM system to the seawater surface gives the apparent ice thickness, or the snow and ice thickness where a snow cover exists. With the use of higher AEM system operating frequencies and appropriate algorithms, we hope to determine the apparent conductivity of the sea ice as well. Then, in principle, through the use of data such as those given in Figure 29, the average brine volume of the ice can be estimated. And from data such as those in Figure 30, an assessment of the mechanical properties of the ice sheet can be made.

Field trials in 1985 included flights over first-year and second-year sea ice as well as a large grounded second-year rubble formation. An example AEM profile over a snow-free, relatively uniform 0.75-m-thick refrozen lead is shown in Figure 54. The profile for the ice is seen to vary in thickness. This variation is believed to be due in part to system noise, the $\approx$ 10-cm accuracy of the laser profilometer, and bird pitch and roll variations. The latter could not be fully accounted for in the bird pendulum potentiometer data. However, the AEM data did give an average thickness for the lead ice of 0.65 m. This result was extremely encouraging. An improved vertical accelerometer and pitch and roll sensor package, reduction of system noise and a more accurate laser profilometer should further improve these results. The average seawater conductivity σ_s was determined to be 3.0 S/m, or about ½ S/m higher than the measured value. Note that the water depth under the ice was also profiled. We did not anticipate this determination being made at this site and thus no direct sounding verification was made.

AEM system profiles were made over a second-year pressure ridge and adjoining low-lying ice. The AEM bird was flown down a 250-m-long track established on the ice. This track

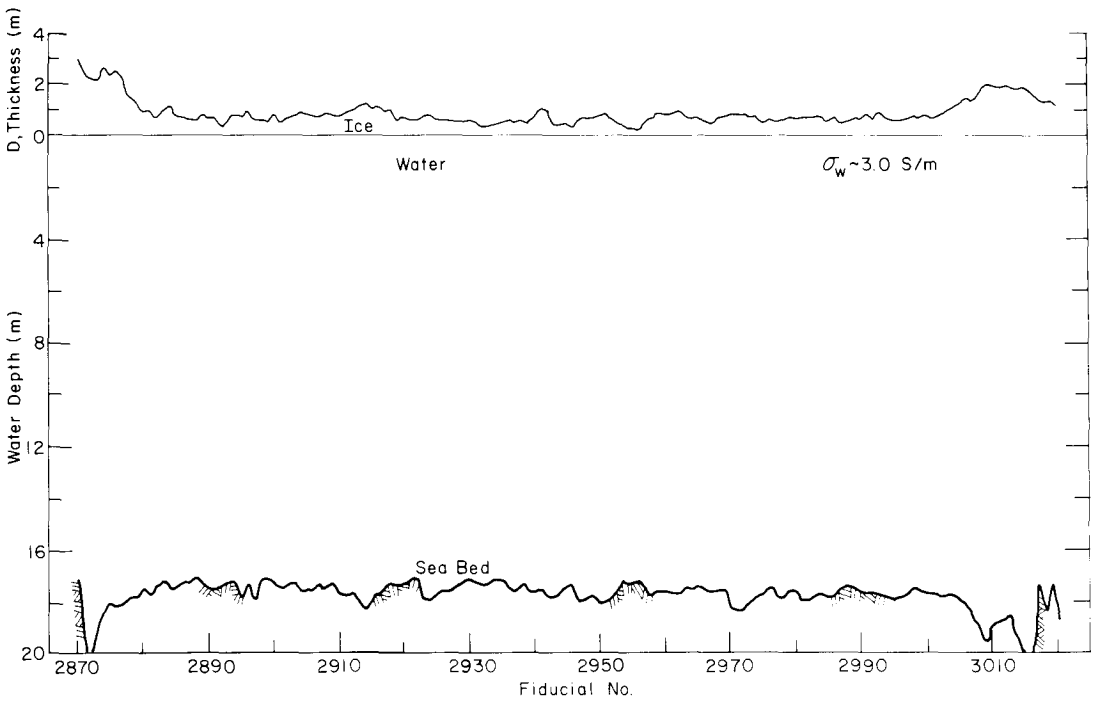

Figure 54. Example profile resulting from AEM sounding over 0.75-m-thick lead ice (from fiducial no. 2890 to 3000). Complete profile is about 4 km long.

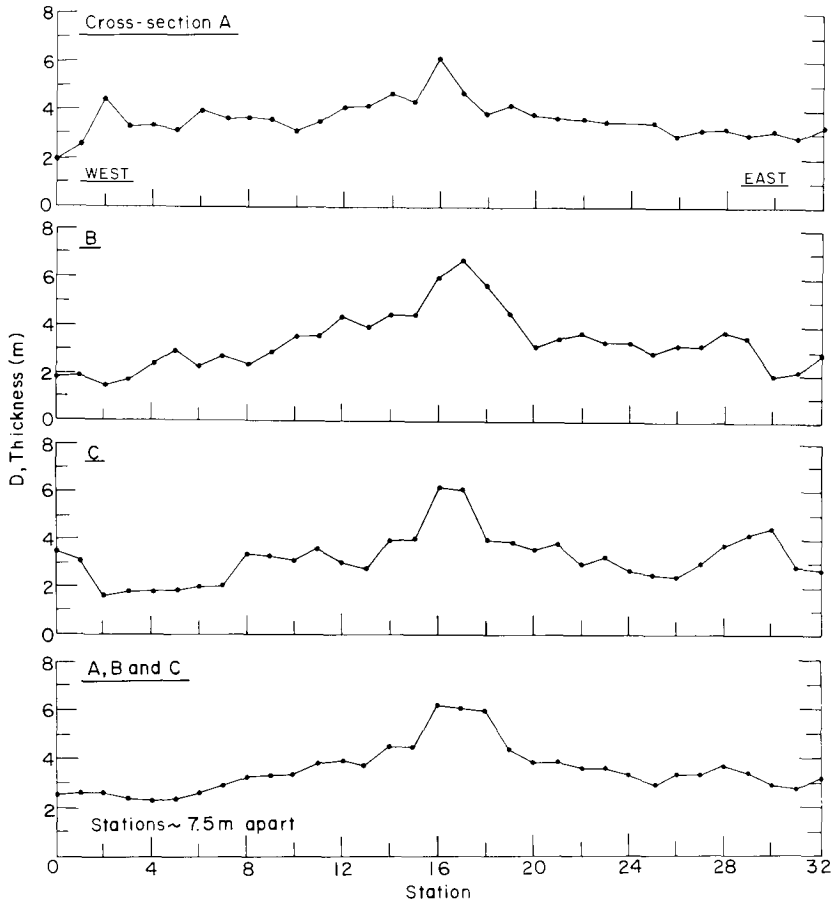

Figure 55. Drill-hole-measured snow and second-year ice thicknesses along the three 250-m-long parallel lines spaced 11½ m apart. Drill hole measurements were made at 7½-m intervals along each line. The three lines formed the track or flight corridor down which the AEM system antenna was flown.

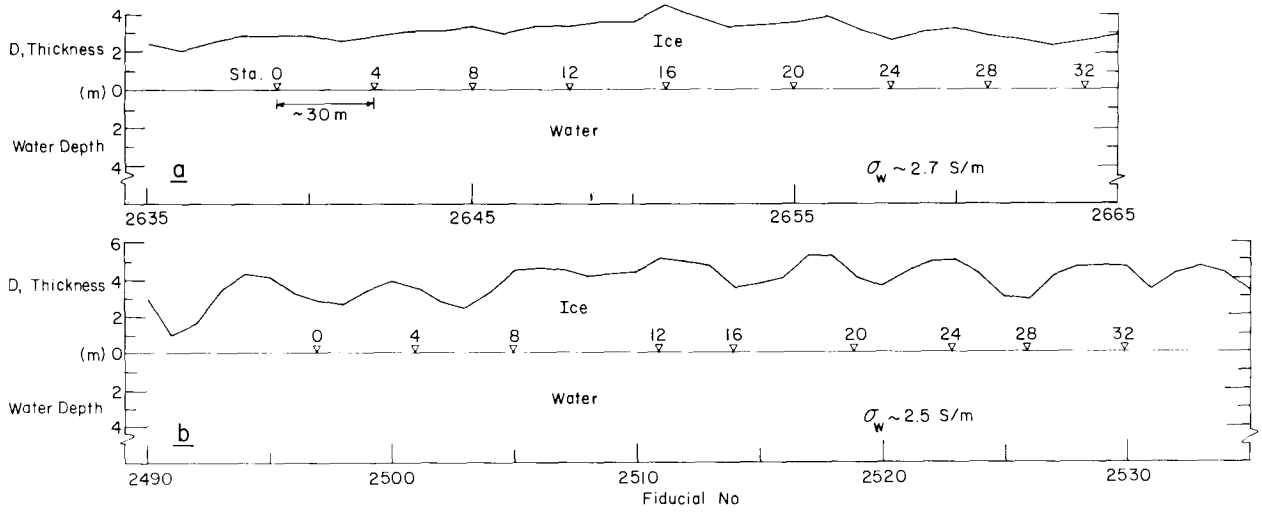

Figure 56. Examples of two AEM profiles run along a track established on second-year sea ice. Distance from first triangular station marker to last is 250 m. Stations relate to those shown in Figure 55.

consisted of three parallel lines spaced 11½ m apart. Snow and ice thicknesses along each line were determined by drill hole measurement. These thickness profiles are presented in Figure 55. The profiles show, as expected, that variations in ice thickness exist between the profiles at each station location. The thickest snow and ice shown occurred at the ridge location. The average snow and ice thickness as determined by drill hole measurement for each profile was 3.54, 3.74 and 3.58 m, for an overall average ice thickness of 3.62 m.

Two example ice thickness profiles obtained with the AEM system are given in Figure 56. There are significant relief differences between the two profiles, and neither clearly shows the thicker ridge ice. Three profiles were run with the 32-kHz coil in the bird and two with the 16-kHz coil. The former profiles gave average ice thicknesses of 4.07, 3.07 and 3.55 m, for an overall average ice thickness of 3.56 m. The average ice thicknesses for the 16-kHz profiles were 3.20 and 3.45 m, for an overall average of 3.32 m. Because there is substantial variation in ice thickness along each of the drill-hole-measured profiles, and because the AEM bird wandered along the flight track, a good correlation between the AEM ice profiles and the drill-hole-measured ice thicknesses cannot be expected. However, the average of all drill-hole-measured snow and ice thicknesses along the track was 3.6 m, versus 3.5 m for the combined AEM data.

The reason why the AEM data did not show the thick ridge ice was the footprint size, and therefore the surface area over which the water surface was integrated into each AEM distance determination. Remember, the AEM system determines the distance from the bird to the water surface, which has depressions in it due to ice bottom relief variations. Our preliminary assessment indicates that the AEM system footprint diameter is about equal to the bird's height. Therefore, the AEM distance to the sea surface is averaged over a relatively large area of undulating relief. This effect smooths out variations in the ice roughness, as occurred in profile a in Figure 58, but does not explain the odd ice thickness variations along profile b.

A profile made over first-year sea ice and a large grounded second-year rubble formation is shown in Figure 57. The latter had formed on a shoal in the fall of 1983, survived the summer break-up and melt season, and was still grounded in place at the time of our May 1985 survey. The shoal on which the formation rested was about 8 m below the sea surface, as indicated by bathymetry charts of the site. The AEM profile indicates that 1½ to 3 m of water

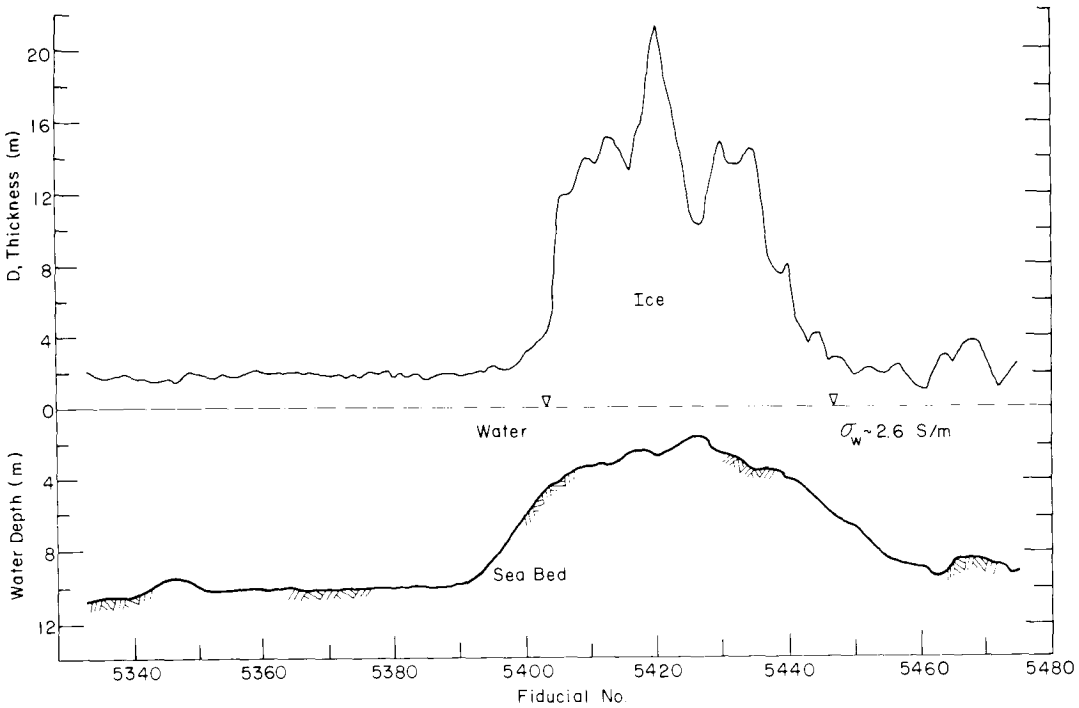

Figure 57. Example of AEM profile run over first-year sea ice and a large grounded second-year rubble formation. The distance between the triangular markers is about ½ km.

existed under the ice rubble. Since the ice formation was grounded, no water should have shown above the shoal. The cause of this ambiguity is believed to be the existence of unfrozen seawater within the submerged ice keel block structure, and/or the AEM system sensing the seawater off to the side of the ice keel. The thickest ice is indicated to be about 22 m thick, which appears reasonable based on ice surface elevation measurements and the apparent shoal depth. The snow-covered first-year sea ice to the left of the feature is shown to average about 1¾ m thick, and the sea bottom to be about 10 m deep at station 5390. Drill hole measurements indicated a very similar snow and ice thickness but a water depth about 1½ m greater. The average AEM-system-determined seawater conductivity was 2.6 S/m, which is in good agreement with measured values.

The AEM system is undergoing specific instrumentation development, and further analytical refinement is in progress to tailor the system to sea ice thickness measurement. The system currently appears to be capable of penetrating sea ice of varying thickness and providing the relative thickness of the ice without being affected, as impulse radar is, by the in situ conductivity of the ice. However, because of the large footprint of the AEM system, relative variations in ice cover relief, such as small pressure ridges and leads, may not be distinguished in the ice profile.

Concluding remarks

The model results presented show the relative variation in the electromagnetic properties of first-year winter sea ice increasing with depth and the effects of ice density, brine volume and temperature on these properties for different ice sheet thicknesses. It was shown that the complex dielectric constant of sea ice also varies with frequency. The electromagnetic property variation with depth for the various ice sheets modeled clearly revealed that the largest losses within first-year winter sea ice occur in the bottom 20% of the sheet.

The relative imaginary dielectric constant values of the sea ice at 5 GHz were shown to be below the values for 1 GHz above a depth of about 0.2 m in the ¾-m-thick ice sheet (Fig. 41). This shift is due to the conductivity of the brine being dominant below about 5 GHz; at higher frequencies, the dielectric relaxation of the brine water is the principal mechanism contributing to the loss. At higher frequencies, where the contribution of brine conductivity to the relative imaginary dielectric constant of the sea ice is no longer significant, it can be expected that the relative imaginary dielectric constant of the sea ice will be proportional to brine volume.

The apparent dielectric constant at 100 MHz for the nine sea ice sheets modeled was found to decrease with increasing ice thickness, following the same trend found for field measurements made at 80 MHz. It was also shown that when the electromagnetic properties of the ¾-m-thick ice sheet were recalculated for a frequency of 80 MHz, the apparent dielectric constant of the model ice sheet agreed with the extrapolated field value. This result indicates that the model electromagnetic properties of cold first-year sea ice are in good agreement with field measurements, and that the analyses presented may be used to estimate the electromagnetic properties of sea ice over a wide range of frequencies and varying ice properties.

When the length of the EM wavelet approaches the "size" of the inclusions in a material, volume scattering can be expected. Therefore, the ϵ''_{rm} values given in Figure 44 for frequencies above, say 10 GHz may vary as a function of inclusion size, geometry and density. The question now is: What inclusion type and geometry will affect ϵ''_{rm}? For example, brine and air pockets exist in sea ice and they may affect ϵ''_{rm} above a frequency of, say, 30 GHz where the wavelength is less than 1 cm. However, larger brine features also exist in the form of brine channels and tubes (Fig. 3). How these and other inclusions interrelate and affect ϵ''_{rm} needs further study.

A significant aspect of the modeling is that it is now possible to estimate first-year winter sea ice thickness using the impulse-radar-determined two-way EM wavelet flight times in the ice. These times can be modeled for the system sounding frequency to be used. In principle, it is also possible to make an assessment of the average brine volume of the ice and thus estimate the strength of the ice sheet, an adventurous prospect to be pursued. However, some of the limitations of impulse radar sounding which were mentioned indicate that this will be an elusive objective to achieve. Indeed, the high conductivity and seawater-filled voids of certain types of sea ice features will preclude an effective assessment of their thickness using impulse radar technology as we know it today.

The airborne electromagnetic survey system discussed appears to have an advantage over impulse radar in that the AEM system is not adversely affected by the conductivity of the sea ice. The limitation of AEM sensing is its large footprint, which has the effect of smoothing local ice thickness variations. Thus, while the system appears to offer a method for determining the relative thickness of an ice floe, it will not provide high-resolution site-specific ice thickness information. Another potential advantage of the AEM system is the ability to determine the apparent conductivity of the ice sheet. In the same vein as the comments made above on impulse radar sounding, from the AEM-system-determined conductivity and ice thickness measurement it may be possible to assess the average brine volume of the ice sheet (Fig. 29) from which an estimate of ice sheet strength can be made. Much remains to be done.

Literature cited

Addison, J.R. (1969) Electrical properties of saline ice. *Journal of Applied Physics,* **40**: 3105–3114.

Anonymous (1968) Proposal for a feasibility study of an airborne technique for measuring sea ice thickness. Geoscience Incorporated, Cambridge, Massachusetts. Proposal submitted to U.S. Navy Oceanographic Office, Washington, D.C.

Assur, A. (1960) Composition of sea ice and its tensile strength. USA Snow, Ice and Permafrost Research Establishment, Research Report 44.

Becker, A., H. Morrison and K. Smits (1983) Analysis of airborne electromagnetic systems for mapping thickness of sea ice. Naval Ocean Research and Development Activity, NORDA Technical Note 216.

Bogorodsky, V.V. (1980) Electromagnetic properties of sea ice. In *Workshop on the Remote Estimation of Sea Ice Thickness.* Center for Cold Ocean Resources Engineering, C-CORE, Publication No. 805, St. John's, Newfoundland.

Cox, G.F.N. and W.F. Weeks (1975) Brine drainage and initial salt entrapment in sodium chloride ice. USA Cold Regions Research and Engineering Laboratory, Research Report 345.

Cox, G.F.N. and W.F. Weeks (1983) Equations for determining the gas and brine volumes in sea ice samples. *Journal of Glaciology,* **29**(102): 306–316.

Cox, G.F.N. and W.F. Weeks (1985) On the profile properties of undeformed first-year sea ice. USA Cold Regions Research and Engineering Laboratory, report prepared for the David Taylor Ship R&D Center (unpublished).

Criminale, W.O., Jr. and M.P. Lelong (1984) Optimum expulsion of brine from sea ice. *Journal of Geophysical Research,* **89**(C3): 3581–3585.

Defant, A. (1961) *Physical Oceanography.* London: Pergamon Press.

Hoekstra, P. and W.T. Doyle (1971) Dielectric relaxation of surface absorbed water. *Journal of Colloid and Interface Science,* **36**(4): 513–521.

Kester, D.R. (1974) Comparison of recent sea water freezing point data. *Journal of Geophysical Research,* **79**(30): 4555–4556.

King, R.W.P. and G.S. Smith (1981) *Antennas in Matter.* Cambridge, Massachusetts: MIT Press.

Kovacs, A. and R.M. Morey (1978) Radar anisotropy of sea ice due to preferred azimuthal orientation of the horizontal c-axes of ice crystals. *Journal of Geophysical Research,* **83**(12): 171–201.

Kovacs, A. and R.M. Morey (1979) Anisotropic properties of sea ice in the 50- to 150-MHz range. *Journal of Geophysical Research,* **84**(C9): 5749–5759.

Kovacs, A. and R.M. Morey (1980) Investigation of sea ice anisotropy, electromagnetic properties, strength and under-ice current orientation. USA Cold Regions Research and Engineering Laboratory, CRREL Report 80-20.

Kovacs, A., R.M. Morey, D.F. Cundy and G. Decoff (1981) Pooling of oil under sea ice. In *POAC 81: Proceedings, Sixth International Conference on Port and Ocean Engineering Under Arctic Conditions,* Laval University, Quebec City, Quebec, Canada. Vol. II, pp. 912–922.

Kovacs, A. and R.M. Morey (1986) Electromagnetic measurements of multi-year sea ice using impulse radar. *Cold Regions Science and Technology,* **12**: 67–93.

Kovacs, A., N.C. Valleau and J.S. Holladay (1987) Airborne electromagnetic sounding of sea ice thickness and sub-ice bathymetry. USA Cold Regions Research and Engineering Laboratory, CRREL Report (in press).

Lake, R.A. and E.L. Lewis (1970) Salt rejection by sea ice during growth. *Journal of Geophysical Research,* **75:** 583.

Langhorne, P.J. and W.H. Robinson (1986) Alignment of crystals in sea ice due to fluid motion. *Cold Regions Science and Technology,* **12**(2): 197–214.

Maykut, G.A. (1985) An introduction to ice in the Polar Ocean. University of Washington Applied Physics Laboratory, Report APL-UW8510.

Morey, R.M., A. Kovacs and G.F.N. Cox (1984) Electromagnetic properties of sea ice. *Cold Regions Science and Technology,* **9**: 53–75.

Morrison, H.F. and A. Becker (1982) Analysis of airborne electromagnetic systems for mapping depth of sea water. University of California at Berkeley, Engineering Geosciences Report.

Nakawo, M. (1983) Measurements on air porosity of sea ice. *Annals of Glaciology,* **4**: 204–208.

Payton, H.R. (1966) Sea ice strength. University of Alaska Geophysical Institute, Report UAG-182.

Schwarz, J. and W.F. Weeks (1977) Engineering properties of sea ice. *Journal of Glaciology,* **19**(81): 499–531.

Sen, P.N. (1984) Grain shape effects on dielectric and electrical properties of rocks. *Journal of Geophysics,* **49**(5): 586–587.

Stogryn, A. (1971) Equations for calculating the dielectric constant of saline water. *IEEE Transactions on Microwave Theory and Techniques,* **19**(8): 733–736.

Timco, G.W. and R.M.W. Frederking (1986) Confined compression tests: Outlining the failure envelopes of columnar sea ice. *Cold Regions Science and Technology,* **12**(1): 13–28.

Tinga, W.R., W.A.G. Voss and D.F. Blossey (1973) Generalized approach to multiphase dielectric mixture theory. *Journal of Applied Physics,* **44**(9): 3897–3902.

Tiphane, M. and J. St-Pierre (1962) Tables de détermination de la salinité de l'eau de mer par conductivité électrique. University of Montreal, Department of Science, Internal Report.

Wang, Y.S. (1979) Crystallographic studies and strength tests of field ice in the Alaska Beaufort Sea. In *POAC 79: Proceedings Fifth International Conference on Port and Ocean Engineering Under Arctic Conditions, University of Trondheim, Trondheim, Norway,* pp. 651–665.

Weeks, W.F. and A.J. Gow (1979) Crystal alignment in the fast ice of arctic Alaska. USA Cold Regions Research and Engineering Laboratory, CRREL Report 79-22.